J. Fluid Mech. (2013), *vol.* 717, *pp.* 134–165.
doi:10.1017/jfm.2012.563

Interaction between feedback aeroacoustic and acoustic resonance mechanisms in a cavity flow: a global stability analysis

Sami Yamouni†, Denis Sipp and Laurent Jacquin

ONERA DAFE, 8 rue des Vertugadins, 92190 Meudon, France

(Received 28 March 2012; revised 22 October 2012; accepted 13 November 2012)

We perform a global stability analysis of a flow over an open cavity, characterized by a Reynolds number, based on the upstream velocity and the cavity length, of 7500. We compute base flows and unstable global modes of the flow for different Mach numbers ranging from 0 to 0.9. In the incompressible regime ($M = 0$), we show that the flow is subject to global instabilities due to Kelvin–Helmholtz instabilities in the shear layer, which become strengthened by a hydrodynamic pressure feedback. The influence of the boundary-layer thickness and of the length-to-depth ratio of the cavity on these shear-layer modes has been investigated. In the compressible regime ($M > 0$), we have shown that all unstable global modes are continuously connected to the incompressible shear-layer modes as $M \to 0$. These shear-layer modes correspond to the beginning of branches of global modes, whose frequencies evolve (as a function of the Mach number), in accordance with the feedback aeroacoustic mechanism (Rossiter, *Tech. Rep.* Aero. Res. Counc. R. & M., 1964). We have also identified branches of global modes behaving in agreement with acoustic resonance mechanisms (East, *J. Sound Vib.*, vol. 3, 1966, pp. 277–287; Tam, *J. Sound Vib.*, vol. 49, 1976, pp. 353–364; Koch, *AIAA J.*, vol. 43, 2005, pp. 2342–2349). At the intersections between both types of branches, the growth rate of the global modes is seen to display a local maximum. Along the aeroacoustic feedback branches, the number of vortical structures in the shear layer is kept constant, while the pressure pattern inside the cavity is conserved along the acoustic resonance branches. We show that both the feedback aeroacoustic and acoustic resonance mechanisms are at play over the entire subsonic regime, from $M = 0$ to $M = 0.9$. At low Mach numbers, we suggest that it is still the feedback aeroacoustic mechanism that selects the frequency, even though the fundamental acoustic resonance mode is also important due to enhancing the response. At higher Mach numbers, we observe that the pressure pattern of the acoustic resonance modes (fundamental acoustic modes, first longitudinal acoustic modes, first longitudinal-depth acoustic modes) inside the cavity determines the directivity of the radiated noise. Links with experimental results are finally discussed.

Key words: cavity flow, compressible flows, instability

1. Introduction

Cavity flows are well known in aeronautics to be an important source of unsteady loads and noise, which can be detrimental to the structure of an airplane for example.

† Email address for correspondence: sami.yamouni@onera.fr

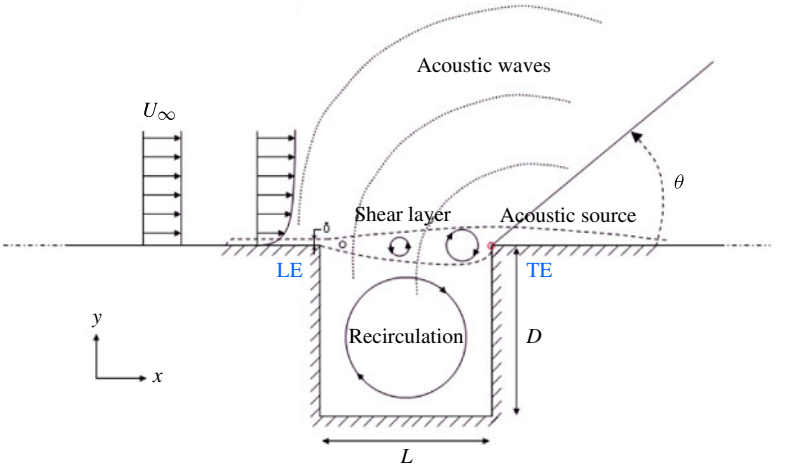

FIGURE 1. Configuration of an unconfined laminar cavity.

To control this phenomenon, it still remains necessary to better understand the leading physical mechanisms. In the case of high-Reynolds-number and high-subsonic-Mach-number flows, Krishnamurty (1956) has observed experimentally that the pressure spectrum displays strong discrete tones associated with strong acoustic radiations. In the case of low-Reynolds-number flows, the same phenomenology has been observed by Rowley, Colonius & Basu (2002), thanks to a two-dimensional direct numerical simulation. In particular, his results showed good agreement between the density fluctuations and Schlieren photographs in an experiment.

In a cavity flow, it is generally acknowledged that two physical mechanisms are at play. First, the feedback aeroacoustic mechanism, described by Rossiter (1964) (figure 1), induces self-sustained oscillations. Small disturbances are amplified along the shear layer by the Kelvin–Helmholtz instability and convected downstream. The impact of these structures upon the cavity trailing edge leads to the formation of acoustic waves travelling upstream up to the sensitive region located at the leading edge. They then excite disturbances at the cavity leading edge to form new structures amplifying along the shear layer. This feedback loop has been described as a shear-layer mode by Rowley *et al.* (2002). Note that at high length-to-depth ratios and high Mach numbers, this mode is no longer seen and a wake mode sets in. Second, acoustic standing-wave resonances occur if the acoustic wavelength is of the same order as the length (or depth) of the cavity. Plumblee, Gibson & Lassiter (1962) first predicted the resonant frequencies of a rectangular cavity theoretically. Later, by neglecting the mean flow effects, Tam (1976) and Koch (2005) obtained acoustic modes for different cavity geometries. Finally, East (1966) was the first to notice that these two mechanisms, feedback aeroacoustic and acoustic resonance mechanisms, may interact and that the feedback aeroacoustic mechanism is enhanced when the characteristic frequencies of both mechanisms match. Tam & Block (1978) stated that a theory combining both mechanisms is still lacking.

The feedback aeroacoustic and acoustic resonance mechanisms are linear in essence. A global linear model, combining both mechanisms, should be able to describe the above mentioned interaction mechanisms (Mery & Casalis 2011). Alvarez, Kerschen & Tumin (2004) built a simplified theory combining propagation models in the central

region of the cavity with scattering models for the end regions. They were able to qualitatively characterize the coupling between the Rossiter modes and the acoustic resonance modes. In this article, we perform a linear stability analysis which is aimed at identifying the eigenvalues and eigenvectors of the linearized compressible Navier–Stokes equations around a given base flow. The configuration is complex here and cannot be described by a weakly non-parallel approach (Monkewitz, Huerre & Chomaz 1993): both the base flow and the eigenvectors explicitly depend on the x and y spatial coordinates and the stability analysis is therefore termed global (Jackson 1987; Theofilis 2003; Sipp *et al.* 2010). Different works have already used global stability analysis of compressible flows, including Crouch, Garbaruk & Magidov (2007) (shock-induced transonic buffet on a NACA0012 aerofoil), Robinet (2007) (shock wave/laminar boundary-layer interaction), Mack, Schmid & Sesterhenn (2008) (flow around a swept parabolic body) or Meliga, Sipp & Chomaz (2010) (axisymmetric wake flows).

The base flow is an equilibrium point of the compressible Navier–Stokes equations and the disturbances are governed by the associated linearized equations. Both the base flow and the eigenvalues/eigenvectors of the stability analysis depend on the Mach number. The involved physical mechanisms are indeed sensitive to compressibility effects. First, the Kelvin–Helmholtz instabilities, which are responsible for the feedback aeroacoustic mechanism, are dampened by compressibility effects (Miles 1958; Pavithran & Redekopp 1989; Meliga 2008). Meliga *et al.* (2010) showed for example that for a base flow that is kept constant, increasing the Mach number induces a stabilization of the Kelvin–Helmholtz instability in wake flows. Concerning the acoustic resonance, the compressibility effects are visible in the frequency of the cavity tones, which evolve as $1/M$ when the Mach number is increased (East 1966).

In the incompressible regime, Sipp & Lebedev (2007) have shown that an open-cavity flow is prone to a super-critical Hopf bifurcation at $Re = 4140$. For super-critical Reynolds numbers, Barbagallo, Sipp & Schmid (2009) showed that 4 unstable global modes exist at $Re = 7500$: the structures of the unstable global modes display a Kelvin–Helmholtz instability on the shear layer and suggest that they may be related to the Rossiter (Rossiter 1964) feedback mechanism, although the results pertain to the incompressible regime. Also, Sarohia (1975) observed two frequency peaks in this regime that match the predictions by the Rossiter mechanism, while Basley *et al.* (2011) experimentally confirmed the existence of the shear-layer mode in the incompressible regime, from time-resolved particle image velocimetry (TR-PIV) measurements. Concerning the cavity dynamics in the compressible regime, Brès & Colonius (2008) also used a global stability analysis at low Reynolds numbers to look for three-dimensional global instabilities in a two-dimensional flow. They found that centrifugal instability inside the cavity is responsible for the existence of three-dimensional instabilities.

The objective of the paper is to characterize the two phenomena leading to the compressible two-dimensional cavity dynamics, the feedback aeroacoustic resonance and the acoustic resonance, using a global stability analysis. In particular, we will try to understand the interaction between both mechanisms, which has already been observed in experimental studies by Block (1976), Rockwell & Naudascher (1978), Ahuja & Mendoza (1995) and Yang *et al.* (2009). From a broader point of view, this article deals with the interaction between hydrodynamic instabilities and acoustic resonance modes. This interaction phenomenon may also be encountered in other configurations such as the Taylor–Culick flow (see Chedevergne, Casalis & Féraille 2006), combustion instabilities (see Candel 1992) or an impinging jet (Rockwell &

Schachenmann 1982): the flow is subject to a hydrodynamic instability (which exists for the incompressible regime) that is enhanced by acoustic resonance mechanisms. As a result, the flow field displays strong responses when the frequencies of the hydrodynamic and acoustic mechanisms match.

In this article, we consider a subsonic, laminar and compressible cavity flow of length-to-depth ratio L/D. We will analyse the influence of compressibility on the cavity dynamics, by varying the Mach number from the incompressible case ($M = 0$) to high subsonic Mach numbers ($M \leqslant 0.9$). The chosen geometry is a two-dimensional cavity (figure 1) similar to that used by Barbagallo *et al.* (2009), except that it is unconfined here. We also choose the same Reynolds number $Re = 7500$, which ensures that the flow is globally unstable in the incompressible limit for $L/D = 1$ (Sipp & Lebedev 2007). The paper is organized as follows. First, we analyse the incompressible regime and retrieve the two-dimensional unstable global modes found in the work by Sipp & Lebedev (2007) and driven by the Kelvin–Helmholtz instability. The effect of important parameters, such as the boundary-layer thickness and the length-to-depth ratio, will be investigated. In § 3, we will show how the eigenvalues of these unstable global modes evolve as the Mach number increases from 0 to 0.9. In § 4, we identify branches of global modes related to the feedback aeroacoustic and acoustic resonance mechanisms. A discussion relating these results to those obtained in experiments is offered in § 5. Section 6 concludes the article.

2. The incompressible regime ($M = 0$)

2.1. *Flow configuration, governing equations and numerical method*

We study the case of an open cavity flow presented in figure 1, characterized by a length-to-depth ratio L/D. Henceforth, we will use the length L of the cavity and the upstream quantity U_∞ as the respective length and velocity scales. The leading and trailing edges of the cavity will respectively be denoted 'cavity LE' and 'cavity TE' henceforth (see figure 1). The flow is characterized by a Reynolds number, based on U_∞ and L, equal to $Re = 7500$. A Cartesian coordinate system has been chosen whose origin is located at the cavity LE. The configuration is characterized by a boundary layer at the cavity LE, whose thickness may be adjusted by selecting the length B of the upstream plate: for this, a slip condition is imposed on ($x < -B, y = 0$) and a no no-slip condition on ($-B \leqslant x \leqslant 0, y = 0$).

In this section, the flow field is governed by the incompressible Navier–Stokes equations formulated as

$$\mathscr{B}(\boldsymbol{q})\partial_t \boldsymbol{q} = \mathscr{R}(\boldsymbol{q}), \tag{2.1}$$

where $\boldsymbol{q}$ represents the aerodynamic field ($\boldsymbol{q} = (u, v, p)^{\mathrm{T}}$). Here $\mathscr{R}$ and $\mathscr{B}$ are differential operators defined as

$$\mathscr{R}(\boldsymbol{q}) = \begin{pmatrix} -\boldsymbol{\nabla u}\cdot\boldsymbol{u} - \boldsymbol{\nabla} p + \dfrac{1}{Re}\Delta \boldsymbol{u} \\ \boldsymbol{\nabla}\cdot\boldsymbol{u} \end{pmatrix}, \tag{2.2}$$

$$\mathscr{B}(\boldsymbol{q}) = \begin{pmatrix} \mathbf{1} & 0 \\ 0 & 0 \end{pmatrix}. \tag{2.3}$$

A finite-element method is used to solve the governing equations (2.1). The unknown (u, v, p) is spatially discretized on an unstructured mesh composed of triangular elements, using P2 elements for the velocity components and P1 elements

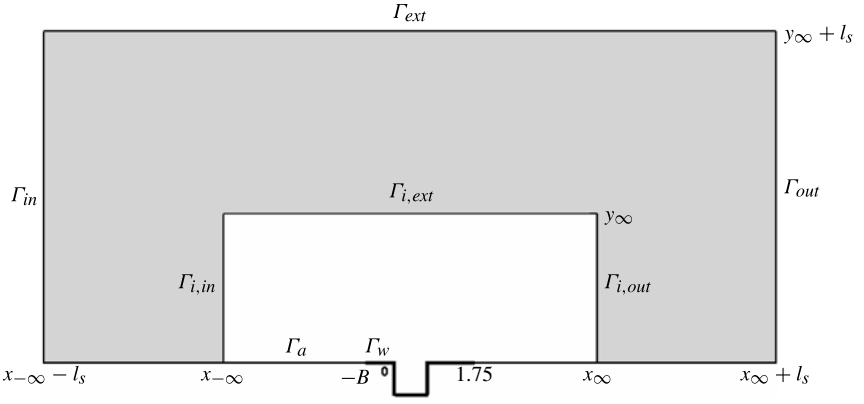

FIGURE 2. Schematic of the computational domain: the white area is the physical domain of interest, padded into a sponge zone, shown as the grey shaded area. A no-slip condition is applied on Γ_w, represented by a thick solid line, while a slip condition is applied on the remaining lower boundary Γ_a.

for the pressure characterized by six and three degrees of freedom, respectively, in one triangular cell. This results in a discretization that is of second order for the velocity unknowns. The resulting sparse matrices are generated with the *FreeFem++* software (http://www.freefem.org). All matrix inversions are performed using a multifrontal sparse LU solver (MUMPS; see Amestoy *et al.* (2001)). Note that, in regions of the flow where the mesh is coarse, an artificial viscosity $\nu_\Delta = \Delta/200$ based on the local cell size Δ is used to stabilize the discretization method: for this, the Reynolds number has been replaced by $\min(Re, 1/\nu_\Delta)$. In regions of the flow where the mesh is fine (for example, in the cavity region and in its vicinity), ν_Δ is really small and the effective Reynolds number $\min(Re, 1/\nu_\Delta)$ is, as expected, equal to Re.

The mesh is described in figure 2. In this section, we only use the inner part (white area), the outer grey shaded region being used later as a sponge zone to damp acoustic fluctuations when compressible equations are considered. Here $\Gamma_{i,in}$, $\Gamma_{i,out}$ and $\Gamma_{i,ext}$ represent the inlet, outlet and upper boundaries, located at $x_{-\infty} = -B - 5$, $x_\infty = 5$ and $y_\infty = 5$, respectively. In the case $B = 0.4$, the mesh comprises 479 772 triangles, which leads to 2 166 792 degrees of freedom for the unknown (u, v, p). On $\Gamma_{i,in}$, we impose a Dirichlet boundary condition $(u, v) = (1, 0)$, on $\Gamma_{i,out}$ a standard outflow condition $(p - Re^{-1}\partial_x u = 0, \partial_x v = 0)$, on Γ_w a no-slip condition $(u, v) = (0, 0)$, on Γ_a $((x \leqslant -B, y = 0)$ and $(x > 1.75, y = 0))$ and on $\Gamma_{i,ext}$ a slip condition $(\partial_y u = 0, v = 0)$.

2.2. *Global stability analysis*

The aerodynamic field $\boldsymbol{q}$ is decomposed into a two-dimensional steady base-flow $\boldsymbol{q}_0 = (u_0, v_0, p_0)^{\mathrm{T}}$ and a disturbance $\boldsymbol{q}_1 = (u_1, v_1, p_1)^{\mathrm{T}}$ of small amplitude ϵ: $\boldsymbol{q} = \boldsymbol{q}_0 + \epsilon \boldsymbol{q}_1$. After introducing this approach into the governing equation (2.1) and linearization, we obtain at the dominant order (see § 2.2.1) the base-flow equation that determines $\boldsymbol{q}_0$ and at the first order (see § 2.2.2) the linearized dynamics that governs the disturbance $\boldsymbol{q}_1$. This incompressible approach has already been used by Sipp & Lebedev (2007) where, in the case of the cylinder flow, the critical Reynolds number $Re_c = 47$ and Strouhal number $St_c \approx 0.12$ (see the reference case by Barkley (2006)) have been recovered precisely.

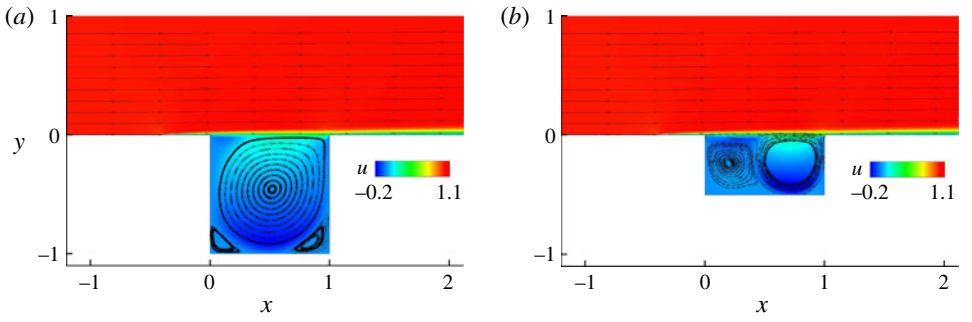

FIGURE 3. Base flow at $Re = 7500$ and $B = 0.4$. Spatial distribution of the streamwise velocity for two different length-to-depth ratios: (*a*) $L/D = 1$ and (*b*) $L/D = 2$.

B	0.4	1.6	6.4	12.5	20
L/θ_0	231	110	52.7	38.9	34.2

TABLE 1. Values of L/θ_0 as a function of the length B of the upstream plate.

2.2.1. *Base flow*

The base flow $\boldsymbol{q}_0$ is a solution of the steady form of the nonlinear equation (2.1):

$$\mathscr{R}(\boldsymbol{q}_0) = \boldsymbol{0}. \tag{2.4}$$

For the parameter regimes under investigation in this article, this solution cannot be obtained by iterating the Navier–Stokes equations over time since the base flow is unstable (we would in fact reach an unsteady periodic regime). We therefore choose to use a standard Newton iteration method to determine the zero of this nonlinear equation: at each iteration, we improve a guess solution $\boldsymbol{q}_0$ by looking for the modification $\delta\boldsymbol{q}_0$ so that $\mathscr{R}(\boldsymbol{q}_0 + \delta\boldsymbol{q}_0) = \boldsymbol{0}$. Linearizing this relation yields: $\delta\boldsymbol{q}_0 = -\mathscr{A}^{-1}(\boldsymbol{q}_0)\mathscr{R}(\boldsymbol{q}_0)$, where $\mathscr{A} = \partial\mathscr{R}/\partial\boldsymbol{q}$ is the linearized differential operator around the current $\boldsymbol{q}_0$.

Figure 3(*a,b*) represent, for $B = 0.4$, the streamwise velocity of the base flows obtained for two cavity geometries: $L/D = 1$ (figure 3*a*) and $L/D = 2$ (figure 3*b*). For $L/D = 1$, the flow shape is similar to the case of Barbagallo *et al.* (2009), presenting a shear layer above the cavity, and a recirculation inside. For $L/D = 2$, the recirculation bubble moves to the right of the cavity leading to the creation of a counter-rotating vortex in the left part of the cavity. Such a pattern has already been observed by Brès & Colonius (2008). The displacement thickness of the boundary layer near the cavity LE is approximately equal to $\delta_0 \approx 0.012$. The Reynolds number based on this length scale is equal to 90. We also computed the momentum thickness θ_0 and checked that the shape factor is equal to $H = 2.6$, which is characteristic of a Blasius boundary layer. This leads to a value of L/θ_0 equal to 231. In table 1, we show how this parameter is modified when the length B of the upstream plate is increased. For $B = 20$, we obtain $L/\theta_0 = 34.2$, which is similar to the values considered in the stability analysis of Brès & Colonius (2008).

2.2.2. *Linear dynamics*

The disturbance $\boldsymbol{q}_1$ is governed by the following linear equation:

$$\mathscr{B}(\boldsymbol{q}_0)\partial_t \boldsymbol{q}_1 = \mathscr{A}(\boldsymbol{q}_0)\boldsymbol{q}_1, \tag{2.5}$$

where $\mathscr{A}$ is the linearized Navier–Stokes operator around $\boldsymbol{q}_0$. The perturbation is then sought in the form of normal modes

$$\boldsymbol{q}_1(x, y, t) = \hat{\boldsymbol{q}}_1(x, y)\mathrm{e}^{(\sigma+\mathrm{i}\omega)t}, \tag{2.6}$$

where the real numbers σ and ω represent the temporal growth rate and frequency of the global mode $\hat{\boldsymbol{q}}_1$, respectively. Substituting (2.6) in (2.5) leads to a generalized eigenvalue problem for $\lambda = \sigma + i\omega$ and $\hat{\boldsymbol{q}}_1$:

$$\mathscr{A}(\boldsymbol{q}_0)\hat{\boldsymbol{q}}_1 = \lambda\mathscr{B}(\boldsymbol{q}_0)\hat{\boldsymbol{q}}_1. \tag{2.7}$$

This problem is solved thanks to the 'Implicitly Restarted Arnoldi method' of the *ARPACK* library (http://www.caam.rice.edu/software/ARPACK/), using a shift and invert strategy (Lehoucq 1995). Complex shift values have been used to obtain the spectrum along the vertical axis of the (σ, ω) plane. In the following, we use the Strouhal number $St = \omega/2\pi$ instead of the frequency ω. The phase of each global mode has been defined by the condition $\mathrm{Im}(\hat{v}_1(x = 0.75; y = 0)) = 0$, while its amplitude has been normalized to the unit kinetic energy $\int_{\Omega_0} |\hat{u}_1|^2 + |\hat{v}_1|^2 \,\mathrm{d}x\,\mathrm{d}y = 1$, where Ω_0 is the domain $(-1 \leqslant x \leqslant 2;\ y \leqslant 0.5)$.

Barbagallo *et al.* (2009) found that four global modes, which exhibit Kelvin–Helmholtz-type instabilities, were unstable in the case $L/\theta_0 = 231$, $L/D = 1$ but for slightly different boundary conditions. In figure 4, we study the effect of the momentum thickness and length-to-depth ratio on this branch of global modes. Figure 4(*a*) is concerned with the case $L/D = 1$, each symbol referring to a different value of L/θ_0. We observe that for $L/\theta_0 = 231$ (filled square symbols), there are four unstable modes, as in the work by Barbagallo *et al.* (2009). Henceforth, we will refer to these global modes as 'the Kelvin–Helmholtz branch' (including the stable modes labelled $k = 1, 6$). As L/θ_0 decreases, the Kelvin–Helmholtz branch becomes progressively stabilized, with marginal stability occurring for L/θ_0 within [52.7; 110]. In particular, if we follow a global mode displaying the same number of structures k in the shear layer, we can see that an increase in the boundary-layer thickness θ_0 leads to a strong decrease in the global mode growth rate. This is related to the classical stabilizing effect of the shear-layer thickness on the Kelvin–Helmholtz instability (the amplification rate of a Kelvin–Helmholtz perturbation is zero when the boundary-layer thickness reaches 20 % of the perturbation wavelength, see Schmid & Henningson (2001)). The same observations have already been made in experimental works (see Sarohia 1977; Rockwell & Knisely 1979; Gharib & Roshko 1987): for a given boundary-layer thickness θ_0, cavity oscillations appear only if the cavity length is greater than a critical value. Also, we note that the increase in θ_0 leads to a slight decrease in the Strouhal number, which reflects the fact that the convection speed of the vortices decreases slightly when the boundary-layer thickness increases. Figure 4(*b*) is dedicated to the effect of the length-to-depth ratio. For this, we have considered two length-to-depth ratios, $L/D = 1$ (filled symbols) and $L/D = 2$ (open symbols), with a thin ($L/\theta_0 = 231$) and a thick boundary layer ($L/\theta_0 = 52.7$). The mode frequencies remain almost the same, whereas the amplification rate is only weakly modified (see in particular low-Strouhal-number modes for $L/\theta_0 = 231$). Generally speaking, these results show that the length-to-depth ratio has only a weak effect on the Kelvin–Helmholtz branch. Case $L/\theta_0 = 52.7$ was chosen here because it coincides with the value used in the work of Brès & Colonius (2008).

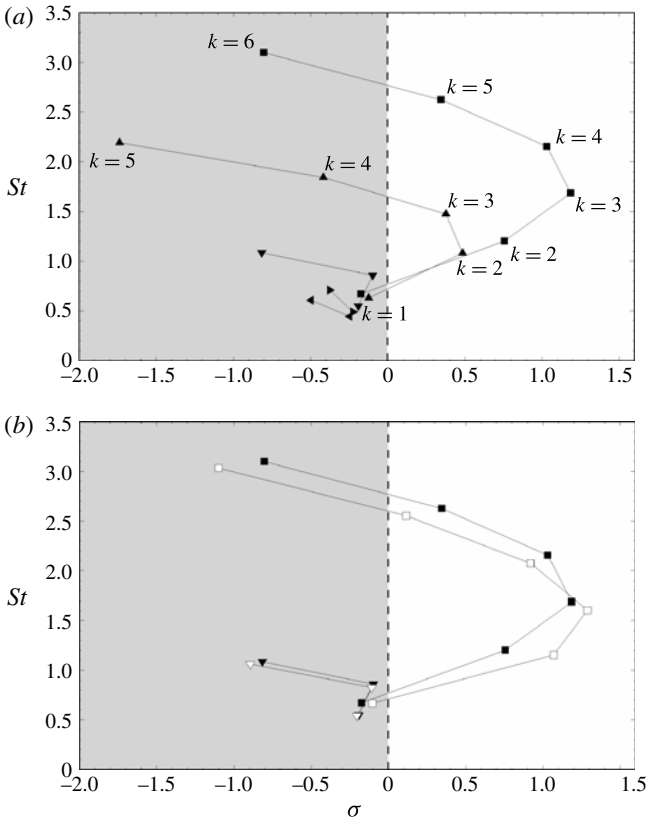

FIGURE 4. Global modes lying on the Kelvin–Helmholtz branch. (*a*) Plot of $L/D = 1$ and different values of L/θ_0: (■), 231; (▲), 110; (▼), 52.7; (►), 38.9; and (◄), 34.2. (*b*) Plot of $L/D = 1$ and $L/\theta_0 = 231$ (■), $L/D = 2$ and $L/\theta_0 = 231$ (□), $L/D = 1$ and $L/\theta_0 = 52.7$ (▼), $L/D = 2$ and $L/\theta_0 = 52.7$ (▽). In (*a*), the numbers k denote the number of structures in the shear layer for the two highest values of L/θ_0.

Henceforth, we will focus on case $L/D = 1$ with a thin boundary layer ($B = 0.4$, $L/\theta_0 = 231$). Hence, the flow is subject to strong Kelvin–Helmholtz-type instabilities. In appendix A, we have shown that the three-dimensional centrifugal-type instabilities (see Brès & Colonius 2008) display weak amplification rates for these parameters. This justifies that we can focus on the two-dimensional Kelvin–Helmholtz modes throughout the rest of the article. For the sake of completeness, we have represented the most unstable global mode in this configuration ($\sigma = 1.19, St = 1.69$) in figure 5. We have shown the real part of the streamwise, cross-stream velocity and pressure in figure 5(*a–c*), respectively. The structure of the mode is similar to that observed in the work by Barbagallo *et al.* (2009): the perturbations are mainly concentrated in the shear layer and their amplitude increases as one gets closer to the cavity TE.

3. Compressible dynamics

3.1. *Flow configuration, governing equations and numerical method*

In this section, we study the effect of compressibility on the dynamics of an open square cavity flow ($L/D = 1$), characterized by a thin boundary layer ($B = 0.4$).

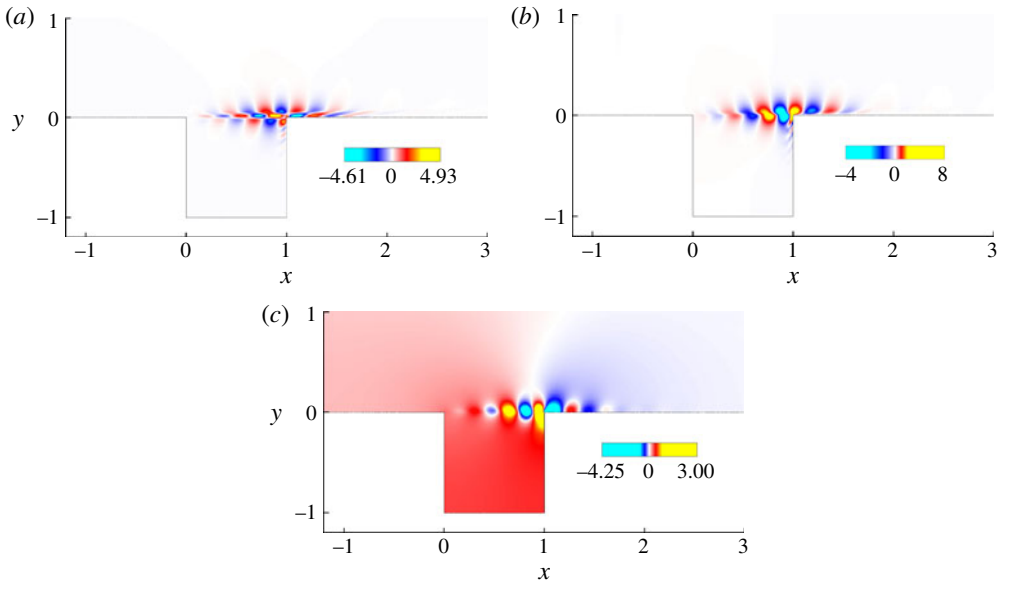

FIGURE 5. Spatial distribution of streamwise velocity (a), cross-stream velocity (b) and pressure (c) in the incompressible regime for the mode ($\sigma = 1.19$, $St = 1.69$).

With respect to § 2, the governing equations $\mathscr{R}$ and variables $\boldsymbol{q}$ have to be modified but the general approach remains the same: determine the base flows, then compute and analyse the unstable eigenvalues/eigenvectors of the Jacobian. We use the length of the cavity L and the upstream quantities U_∞, ρ_∞ and T_∞ as the respective length, velocity, density and temperature scales. As before, the Reynolds number is chosen equal to $Re = 7500$ and the Mach number M ranges between $M = 0.04$ (a value close to the incompressible regime) and $M = 0.9$ (high subsonic compressible regime), these parameters being based on the free stream quantities ($Re = U_\infty L\rho_\infty/\mu$ and $M = U_\infty\sqrt{\rho_\infty}/\sqrt{\gamma p_\infty}$, with μ as the constant dynamic viscosity and p_∞, the free stream pressure). The flow field is governed by the unsteady compressible Navier–Stokes equations. From now on, $\boldsymbol{q}$ represents the aerodynamic field ($\boldsymbol{q} = (\rho, u, v, T)^{\mathrm{T}}$), the pressure having been eliminated using the perfect gas state equation (Meliga *et al.* 2010), while $\mathscr{R}$ and $\mathscr{B}$ denote

$$\mathscr{R}(\boldsymbol{q}) = \begin{pmatrix} -\boldsymbol{u}\cdot\boldsymbol{\nabla}\rho - \rho\boldsymbol{\nabla}\cdot\boldsymbol{u} \\ -\rho\boldsymbol{\nabla}\boldsymbol{u}\cdot\boldsymbol{u} - \dfrac{1}{\gamma M^2}\boldsymbol{\nabla}(\rho T) + \dfrac{1}{Re}\boldsymbol{\nabla}\cdot\tau(\boldsymbol{u}) \\ -\rho\boldsymbol{u}\cdot\boldsymbol{\nabla}T - (\gamma-1)p\boldsymbol{\nabla}\cdot\boldsymbol{u} + \gamma(\gamma-1)\dfrac{M^2}{Re}\tau(\boldsymbol{u}) : \boldsymbol{d}(\boldsymbol{u}) + \dfrac{\gamma}{PrRe}\nabla^2 T \end{pmatrix}, \quad (3.1)$$

$$\mathscr{B}(\boldsymbol{q}) = \begin{pmatrix} 1 & \boldsymbol{0} & 0 \\ 0 & \rho\boldsymbol{I} & 0 \\ 0 & \boldsymbol{0} & \rho \end{pmatrix}. \quad (3.2)$$

Here $\gamma = 1.4$ designates the heat capacity ratio of air and $Pr = 0.72$ is its Prandtl number. The strain and stress tensors are $\boldsymbol{d}(\boldsymbol{u}) = (\boldsymbol{\nabla}\boldsymbol{u} + \boldsymbol{\nabla}\boldsymbol{u}^{\mathrm{T}})/2$ and $\boldsymbol{\tau}(\boldsymbol{u}) = -(2/3)(\boldsymbol{\nabla}\cdot\boldsymbol{u})\boldsymbol{I} + 2\boldsymbol{d}(\boldsymbol{u})$, respectively.

Similarly to § 2, we use finite elements to solve the governing equation (2.1). To stabilize the discretization method, a diffusion term proportional to $\nu_\Delta = \Delta/200$ has been added in the ρ equation, while the Reynolds number appearing in the diffusion part of the velocity–temperature equations has been replaced by $\min(Re, 1/\nu_\Delta)$.

The mesh is presented in figure 2. This time, the grey shaded area is taken into account: Γ_{in}, Γ_{out} and Γ_{ext} now represent the inlet, outlet and upper boundaries, respectively, where we impose the following Dirichlet boundary condition: $(\rho, u, v, T) = (1, 1, 0, 1)$. Here Γ_w, represented by a thick solid line, designates the cavity wall, which is assumed adiabatic: $(u, v) = (0, 0)$, $\partial_n T = 0$ with ∂_n referring to the wall normal derivative. Since we are in the (ρ, u, v, T) formulation, we also need a boundary condition for the ρ equation. Similarly to Crouch *et al.* (2007, 2009), we impose $\partial_n \rho = 0$, which is deduced from $\partial_n p = 0$, $\partial_n T = 0$ and the linearization of the perfect gas equation $p = \rho T$. Note that $\partial_n \rho = 0$ is only an approximate boundary condition since no boundary condition is actually required for the ρ variable. Yet, for high-Reynolds-number flows, this approximation is valid. This has been checked numerically by comparing results obtained with and without the boundary condition on ρ. A slip condition is applied on boundary Γ_a ($(x \leqslant -0.4, y = 0)$ and $(x > 1.75, y = 0)$): $\partial_n \rho = 0$, $\partial_n u = 0$, $v = 0$, $\partial_n T = 0$.

In the free stream, acoustic waves are damped to a negligible level thanks to a sponge zone, which has been represented schematically by the grey shaded area in figure 2. This avoids possible reflections of acoustic and vortical fluctuations on the boundaries of the mesh (Colonius 2004). Following Rowley *et al.* (2002), we added on the right-hand side of the governing nonlinear equations (2.1), the damping term $-\beta(x, y)(\boldsymbol{q} - \boldsymbol{q}_{fs})$, where $\boldsymbol{q}_{fs}$ designates the free stream quantity $(1, 1, 0, 1)^{\mathrm{T}}$ (see appendix B). We choose the following damping function $\beta(x, y)$:

$$\beta(x, y) = 0 \qquad \text{if } x_{-\infty} \leqslant x \leqslant x_\infty \text{ and } y \leqslant y_\infty, \tag{3.3a}$$

$$\beta(x, y) = \left|1 - \frac{1}{M}\right| f(x_{-\infty}, x) \qquad \text{if } x < x_{-\infty} \text{ and } y \leqslant y_\infty, \tag{3.3b}$$

$$\beta(x, y) = \left|1 + \frac{1}{M}\right| f(x, x_\infty) \qquad \text{if } x > x_\infty \text{ and } y \leqslant y_\infty, \tag{3.3c}$$

$$\beta = \beta(x, y_\infty) + \left|\frac{1}{M}\right| f(y, y_\infty) \qquad \text{if } y > y_\infty \tag{3.3d}$$

where f is the function defined by

$$f(a, b) = 2\alpha \frac{(a - b)}{l_s^2}. \tag{3.4}$$

Here $x_\infty = 100$, $x_{-\infty} = -50$, $y_\infty = 33$ designate the coordinates of the beginning of the sponge zone, while $l_s = 150$ is its length. The value of α was chosen equal to four. Note that a progressive grid stretching from the cavity to the limits of the computational domain acts as an additional dissipation mechanism to damp the fluctuations.

The unknown (ρ, u, v, T) is spatially discretized on an unstructured mesh composed of triangular elements. We use (P1, P2, P2, P1) elements for the (ρ, u, v, T) unknown. We use a mesh made up of 1 119 022 triangles, leading to 5 610 144 degrees of freedom for the unknown (ρ, u, v, T). We have checked that our results converge by varying these parameters and by using different spatial discretizations ((P2, P2, P2, P2), (P1, P2, P2, P1) and (P1, P1b, P1b, P1)) (see appendix C).

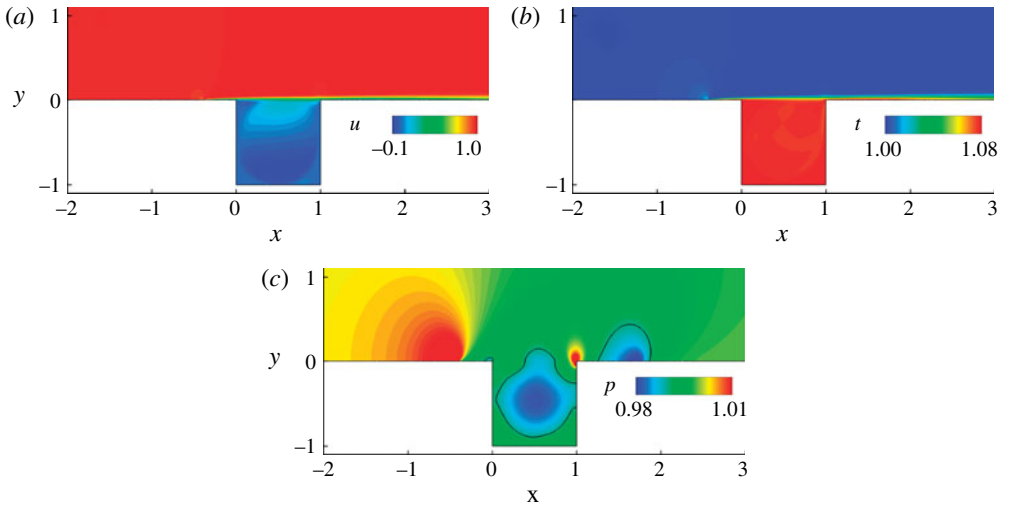

FIGURE 6. Base flow at $Re = 7500$ and $M = 0.7$. Spatial distribution of streamwise velocity (a), temperature (b) and pressure ($p_0 = \rho_0 T_0$) (c). The solid line in (c) is an isocontour of the pressure ($p_0 = 0.99$).

3.2. *Base flow*

The base flow $\boldsymbol{q}_0$ is a solution of the nonlinear equation (2.4), with $\mathscr{R}$ and $\mathscr{B}$ given in (3.1) and (3.2), including the damping term given in (3.3). Using the same Newton iteration method as in § 2, we compute base flows for Mach numbers varying from $M = 0.04$ to $M = 0.9$. Figure 6 represents the base flow visualized through its streamwise velocity (a), its temperature (b) and its pressure (c) at Mach number $M = 0.7$. The flow shape is similar to the incompressible case (see figure 3), presenting a shear layer at the cavity mouth, and a recirculation inside. In figure 6(c), observing the isocontour line of pressure $p_0 = 0.99$, it can be seen that the pressure is nearly constant inside the cavity and across the shear layer. Considering the perfect gas state equation, the increase of temperature seen inside the cavity (figure 6b) is therefore balanced by a decrease in the density. The recirculation bubble is also highlighted in figure 6(c) by a low-pressure region inside the cavity. The high- and low-pressure regions located upstream and downstream from the cavity coincide with the beginning and end of the no-slip boundary Γ_w (see figure 2). Finally, as usual, a high-pressure region is seen at the cavity TE. The displacement boundary-layer thickness only weakly depends on the Mach number (see appendix D). We obtain, as in the incompressible case, values of L/θ_0 equal to 231.

3.3. *Linear dynamics*

The unstable global modes are governed by (2.7), with $\mathscr{A}$ and $\mathscr{B}$ obtained by the linearization of (3.1) and (3.2), including the damping term of (3.3). We have represented the unstable eigenvalues in the (σ, St) plane for various Mach numbers in figure 7(a): the filled square, open diamond, open gradient and open circle symbols refer to the results pertaining to $M = 0$, $M = 0.1$, $M = 0.5$ and $M = 0.9$, respectively. The results for $M = 0$ stem from the incompressible study (§ 2). The spectrum for $M = 0.1$ displays four unstable global modes, as in the incompressible regime, but the amplification rates are higher and the frequencies slightly lower. Note that the

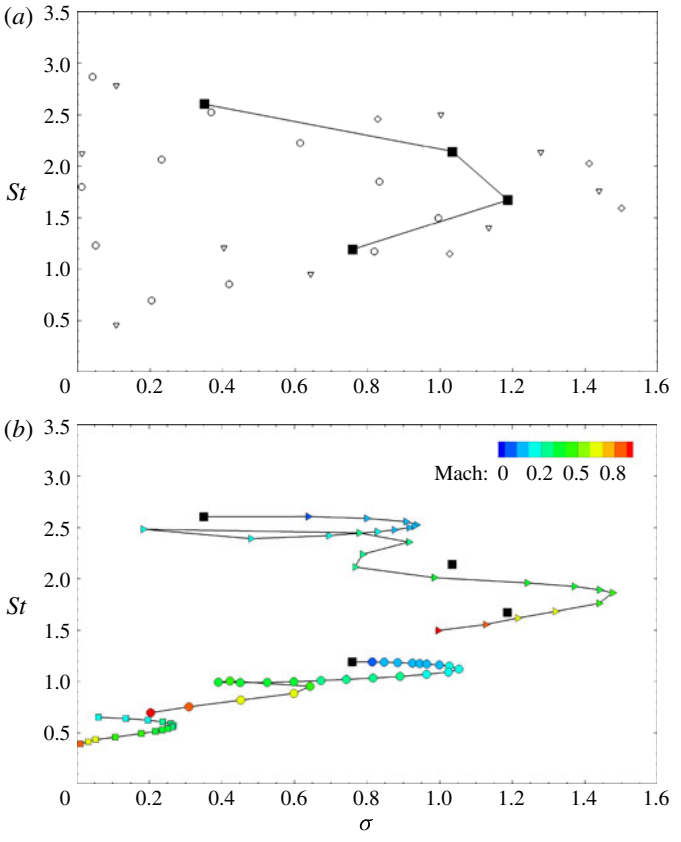

FIGURE 7. (*a*) Global spectrum for flow over a cavity at $Re = 7500$, for: (■), $M = 0$; (◇), $M = 0.1$; (▽), $M = 0.5$; (○), $M = 0.9$. (*b*) Global spectrum with three selected trajectories obtained by continuity. Each trajectory is depicted with different symbols.

differences in amplification rates between the incompressible regime $M = 0$ and the case $M = 0.1$ are quite significant: for the sake of comparison, we recall that, in the case of a compressible axisymmetric bluff-body, Meliga *et al.* (2010) showed that the unstable eigenvalues at $M = 0.1$ were nearly identical to those at $M = 0$. We recall that the Kelvin–Helmholtz instabilities, which amplify perturbations along the shear layer of the open cavity, are at the origin of the instability. Miles (1958), Pavithran & Redekopp (1989) and Meliga *et al.* (2010) have shown that the increase in the Mach number generally dampens shear instabilities. Hence, at first glance, the increase in the amplification rate with the Mach number observed here appears as a surprise. Returning to figure 7(*a*), it is seen that, for higher Mach numbers, the number of unstable modes increases up to 9 for $M = 0.5$ and 11 for $M = 0.9$, which means that the increase in Mach number renders some stable modes unstable. At the same time, the amplification rates of the four above-mentioned unstable global modes eventually decrease for higher Mach numbers, following the general trend described by Miles (1958) and Pavithran & Redekopp (1989). As a conclusion, it seems that the trajectories of the unstable eigenvalues (as a function of the Mach number) in the (σ, St) plane are quite complex.

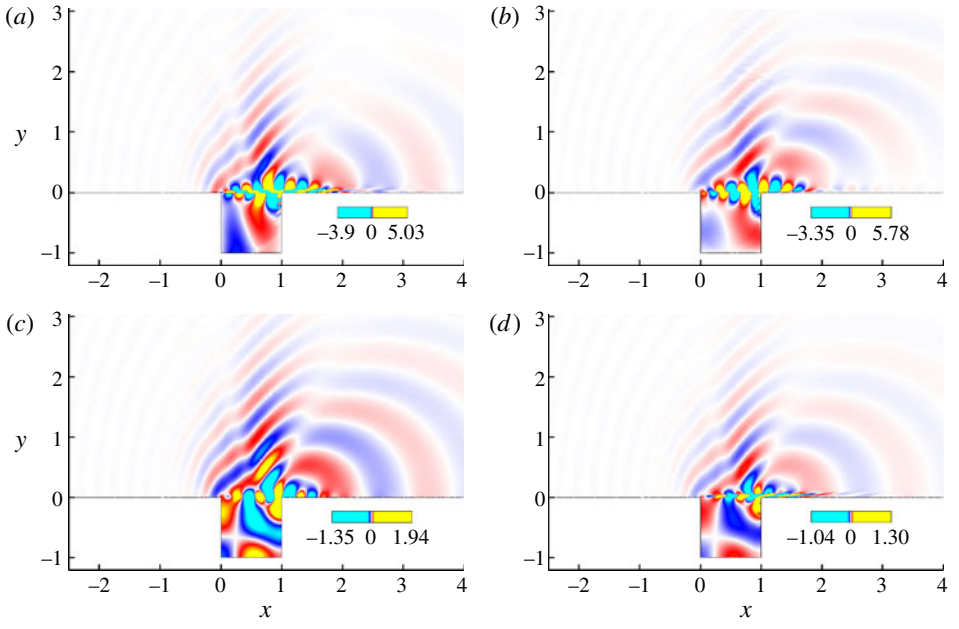

FIGURE 8. Spatial distribution of streamwise velocity (a), cross-stream velocity (b), pressure (c) and temperature (d) at $M = 0.7$ for mode ($\sigma = 1.47$, $St = 1.86$).

Figure 7(b) shows three different eigenvalue trajectories parameterized by the Mach number in the (σ, St) plane: two trajectories starting at the lowest and highest incompressible unstable modes (black square symbols) and one at a very low Strouhal number. A different symbol is used for each trajectory and the colours of the symbols indicate the Mach number: blue for small Mach numbers ($M = 0$), red for high Mach numbers ($M = 0.9$). For the sake of clarity, the other trajectories have not been presented here, but will be described henceforth, their evolution being very complicated. The trajectory starting at the incompressible eigenvalue of the highest frequency (right triangle symbols) displays three local maxima for the amplification rate, with a Strouhal number decreasing from $St = 2.6$ at $M = 0$ to $St = 1.5$ for $M = 0.9$. Moreover, by observing the same trajectory, the increase in the amplification rate with the Mach number can be very large: it is equal to $\sigma = 0.18$ for $M = 0.175$ and $\sigma = 1.47$ for $M = 0.4$.

A typical unstable global mode is shown in figure 8. Figure 8(a–d) represent the real part of the streamwise velocity, cross-stream velocity, pressure and temperature, respectively, of the global mode characterized by $M = 0.7$ and ($\sigma = 1.21$, $St = 1.62$). This mode belongs to the right triangles trajectory. The pressure component has been computed using $\hat{p}_1 = \rho_0 \hat{T}_1 + \hat{\rho}_1 T_0$. As in the incompressible case (see § 2), it is seen that the perturbations are most strongly located on the shear layer, which indicates that the eigenmode is obviously related to the Kelvin–Helmholtz instability. The pressure and temperature fluctuations are of the same order of magnitude as the velocity fluctuations, which shows that the compressibility effects are strong. Also, the eigenmode radiates acoustic waves in the free stream, characterized by a longer wavelength downstream from the cavity than upstream. This stems from the fact that acoustic waves propagate at different speeds in the downstream ($c = 1 + 1/M$) and

upstream ($c = 1-1/M$) directions. The pressure fluctuation level at point ($x = 1$; $y = 2$), which is located in the free stream region, is three orders of magnitudes lower than the maxima occurring in the shear layer. Inside the cavity, the pressure pattern displays two nodes in the x direction and one node in the y direction, while three corotative vortices are seen in the shear layer. These features will be explained below.

4. Physical interpretation of the effect of compressibility on unstable modes

In this section, we will try to understand the complex trajectories of the eigenvalues as a function of the Mach number that have been described in § 3.1. First (§ 4.1), we will recall two basic phenomena that occur in compressible cavity flows: the feedback aeroacoustic mechanism presented by Rossiter (1964) and the acoustic resonance mechanism presented by Plumblee *et al.* (1962). Henceforth, these mechanisms will respectively be called mechanism I and mechanism II. Second (§ 4.2), we will show that the complex trajectories may be well explained by these two mechanisms. In particular, when their frequencies match, a maximum local growth rate is observed in the trajectories of the eigenvalues. The link between the unstable global modes obtained in the incompressible regime and those obtained for $M > 0$ will be discussed in § 4.3. We will finally analyse the shape of the global modes and their acoustic directivity as a function of the Mach number (§ 4.4).

4.1. *The feedback aeroacoustic and acoustic resonance mechanisms*

Rossiter (1964) showed that the oscillation frequency observed in open compressible cavity flows is given by

$$St_1 = \frac{j - \gamma}{\dfrac{1}{\kappa} + M} \tag{4.1}$$

where $j = 1, 2, 3, \ldots$ is a mode number, M is the Mach number, κ is the ratio between the convection speed of the vortices and the free stream velocity and γ is a factor accounting for the lag time between the impact of a vortex on the cavity TE and the emission of a sound pulse. Physically, this relation states that the travelling time of the vortices in the shear layer and of the backward travelling acoustic waves is synchronized. Bilanin & Covert (1973) improved this model by precisely modelling the Kelvin–Helmholtz instability mechanism that occurs in the shear layer considered as a thin vortex sheet. They used an acoustic line source at the downstream corner to model the acoustic reflections on the cavity walls. Later, Block (1976) introduced the length-to-depth ratio L/D in this model by considering the vertical displacement of the shear layer and its impact on the acoustic pressure at the cavity LE and TE. This formula is written as

$$St_2 = \frac{j}{\dfrac{1}{\kappa} + M\left(1 + \dfrac{0.514}{L/D}\right)} \tag{4.2}$$

where L and D are the length and depth of the cavity, respectively. Henceforth, mechanism I will be described by this equation.

The acoustic resonance mechanism (mechanism II) occurs when the wavelength of the acoustic wave is close to the cavity dimensions (L or D) or smaller (Rockwell & Naudascher 1978). Either longitudinal or transversal standing waves may be observed that are characterized by specific discrete frequencies. Following Tam (1976)

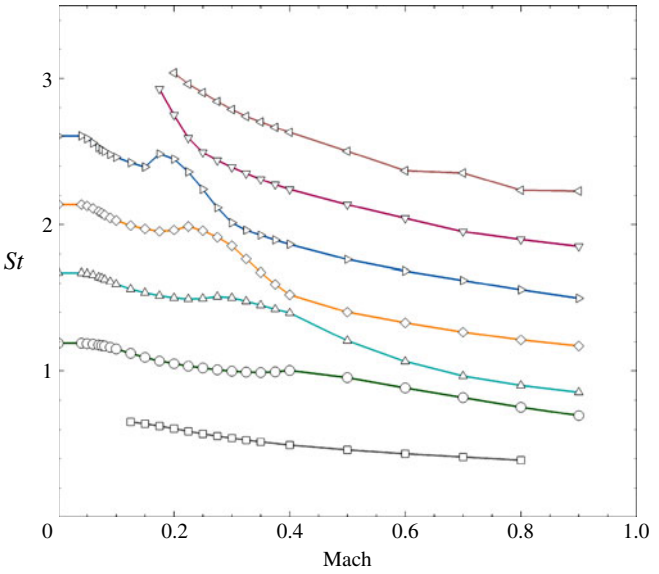

FIGURE 9. (Colour online) Unstable modes obtained by the global stability analysis in the (M, St) plane. The same symbols as in figure 7(*b*) have been used. Only the modes lying on the Kelvin–Helmholtz branch have been represented here. Note that additional unstable modes exist, which display very small amplification rates: these modes may refer to acoustic modes that became unstable through some coupling and have not been considered here due to their weak amplification rates.

and Koch (2005), we can identify the acoustic resonance modes by describing their pattern with the number of pressure nodes in the x and y directions, using the pair (m, n) (with $m, n = 0, 1, 2, \ldots$). Both authors studied the case of zero mean flow with a radiation condition far away from the open end of the cavity. In the case of deep cavities, East (1966) tried to take into account the effect of a free stream Mach number. He observed from the theoretical results of Plumblee *et al.* (1962) that the frequency of the fundamental resonant mode ($m = 0, n = 0$) is governed by

$$St_3 = \frac{0.25}{M\left\{1 + 0.65\left(\frac{L}{D}\right)^{0.75}\right\}}. \tag{4.3}$$

In this paper, we study the particular case $L/D = 1$. This is the limiting case between deep and shallow cavities. We will compare our results with the work of Koch (2005), who also discussed this configuration but in the case of zero mean flow.

4.2. *Identification of both mechanisms by analysing the trajectories of the eigenvalues*

In figure 9, the unstable trajectories, including those shown in figure 7(*b*), have been plotted in the (M, St) plane. This means that the growth rate varies along each curve. We observe that all trajectories are clearly identified and that the frequency on each curve generally decreases with the Mach number.

In figure 10, these trajectories have been represented in the (M, σ) plane, the Strouhal number varying along each curve. Figure 10(*a–f*) correspond to the curves in figure 9, from the lowest to the highest Strouhal numbers, respectively. The

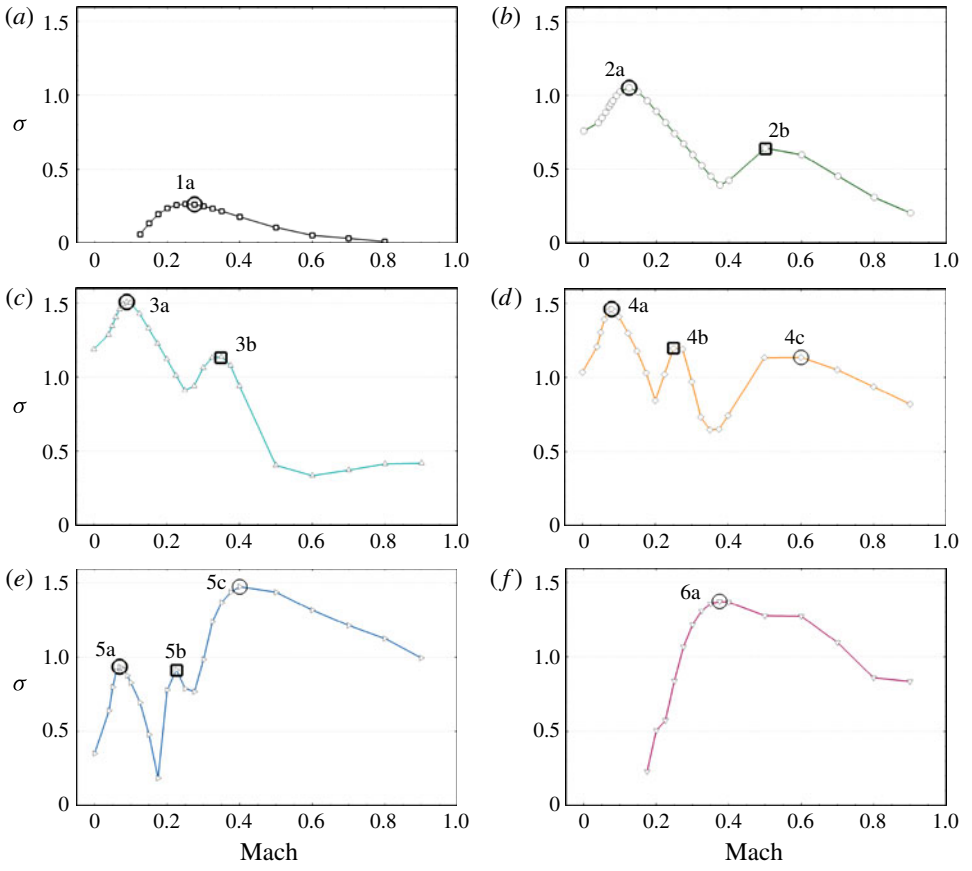

FIGURE 10. (Colour online) Spectra representing the growth rate of the unstable modes as a function of Mach number for each mode trajectory. Big open symbols show the local maxima of the growth rate.

left triangle trajectory at a higher Strouhal number has not been represented. We observe that the growth rates decrease at high Mach numbers, in agreement with the general trend described by Miles (1958) and Pavithran & Redekopp (1989). Yet, for intermediate Mach numbers, each trajectory is rather erratic and displays one or multiple local maxima in the growth rate. These maxima have been identified by large open symbols labelled 1a, 2a, 2b, ...

We will now analyse the structure of the eigenmodes associated with the modes 1a, 2a, 2b.... In figure 11, we have represented the isocontours of the real part of the pressure fluctuation for all of these modes. Recall that the phase of each global mode has been fixed by the condition $\mathrm{Im}(\hat{v}_1(x = 0.75, y = 0)) = 0$ while its amplitude has been normalized as mentioned in § 3.1. This induces, in particular, the imaginary structures to exhibit a vortical structure centred at $(x = 0.75, y = 0)$. We observe that the global modes on a given line display the same number of vortical structures in the shear layer (the number of pressure minima). For example, global mode 1a exhibits one vortex in the shear layer, global modes 2a and 2b exhibit two vortices and global modes 3a, 3b, 4c exhibit three vortices. This suggests that the global modes belonging to a same line all belong to a same branch characterized by the number k of structures

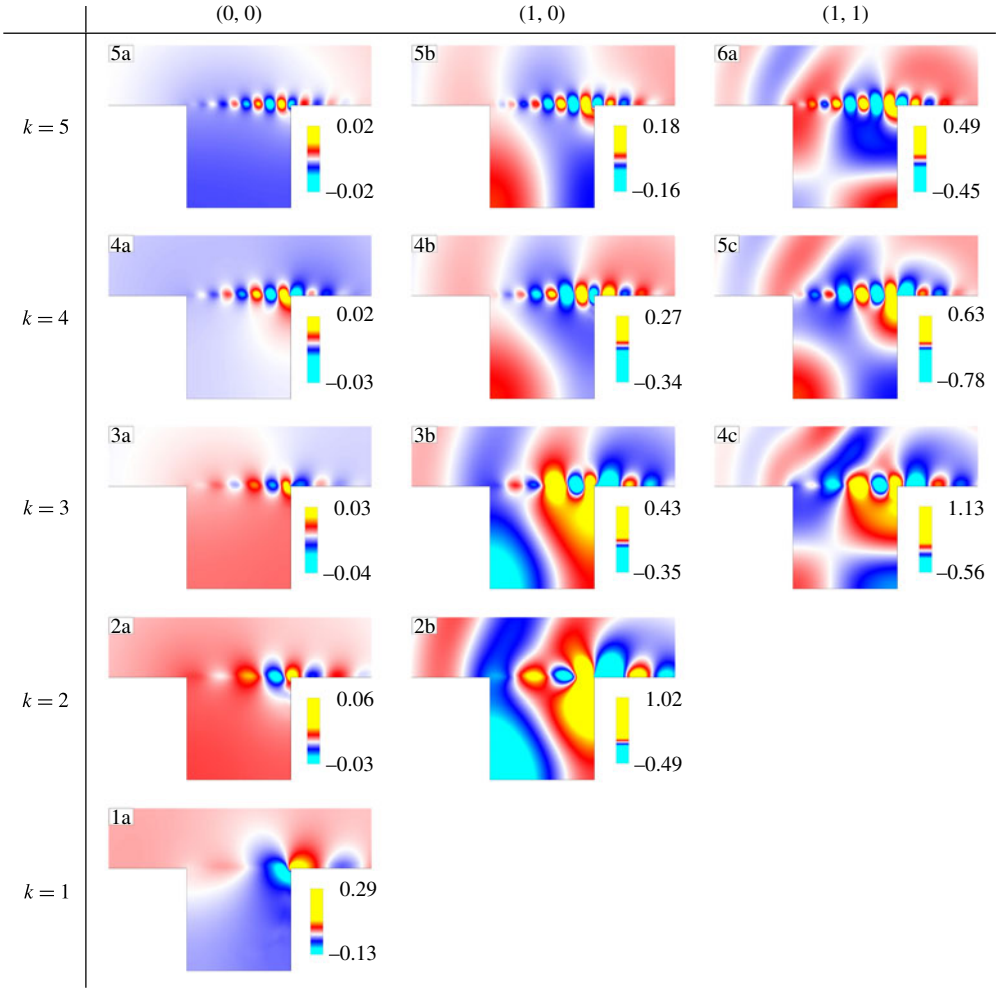

FIGURE 11. Spatial distribution of pressure for the modes of local maximum growth rate. Here k refers to the number of structures in the shear layer and the pairs (m, n) refer to the number of pressure nodes inside the cavity, as introduced by Tam (1976) and Koch (2005). The number (ij) in each figure refers to figure 10. Only the real part of the modes is shown. See the supplementary movies available at http://dx.doi.org/10.1017/jfm.2012.563 where pressure isocontours evolve over time over three time periods (*mode*_4a.*avi*, *mode*_4b.*avi* and *mode*_5c.*avi*).

in the shear layer. This has been even more exemplified in figure 12, where these branches have been highlighted by grey shaded circles ($k = 1, 2, 3, 4, 5$). We observe several branch switching phenomena as introduced by Craik (1988). Modes 3a, 3b and 4c all belong to branch $k = 3$. Comparing with figures 9 and 10, we can see that modes 3a and 3b belong to the trajectory with triangles while mode 4c belongs to the trajectory with diamonds. This is also called an interchange of trajectories in the literature. The location of branch switching is approximately obtained near eigenmodes 2b, 3b, 4b, 5b where the growth rate is locally a maximum.

We now compare the location of the k branches with the aeroacoustic feedback mechanism. For this, we have also represented in figure 12 the frequencies given

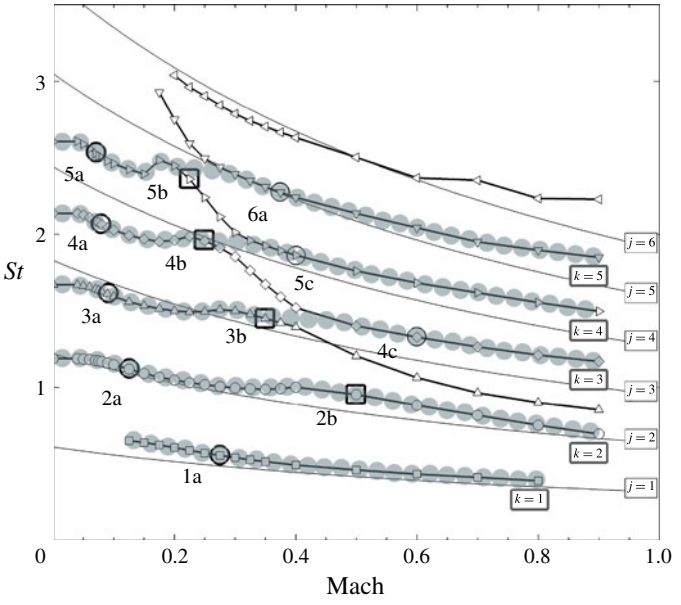

FIGURE 12. Unstable mode trajectories with a constant number of structures (k) in the shear layer (grey shaded circles). The large open symbols refer to the global modes displaying a local maximal growth rate (see figure 10) and the black solid lines are mechanism I branches (equation (4.2)).

by (4.2) with $\kappa = 0.61$ for mode numbers j varying from one (lower black solid line) to six (upper black solid line). This value has already been used in earlier studies (see Koch 2005) and also corresponds to the value making the curves of mechanism I match those of branches $k = 1$ and 2 as best as possible. We observe an excellent agreement for the two lowest modes, which shows that the dynamics related to these global modes is governed by mechanism I. In particular, it explains the decrease in the Strouhal number for increasing Mach numbers, which was observed in figure 7(*b*). For higher Strouhal numbers, a progressive shift between the curves and the grey shaded circles is seen. Finally, we note that the four unstable global modes in the incompressible limit $M = 0$ coincide with the limiting values of the curves associated with mechanism I: this shows that the Rossiter mechanism is also valid in the incompressible regime $M = 0$, but with the pressure feedback being instantaneous (hydrodynamic feedback). These modes have been observed experimentally by Sarohia (1975) and Basley *et al.* (2011) in the incompressible regime. Also, it is seen that branch $k = 1$ only starts being unstable for $M \geqslant 0.1$: for $M = 0$, this mode was already shown to be stable (mode M1 in figure 10 in the work by Barbagallo *et al.* (2009)).

Returning to figure 11, we also observe that in a given column, a common pressure pattern is conserved inside the cavity. In the first column, modes 1a, 2a, 3a, 4a and 5a display a uniform structure inside the cavity. In the second column (modes 2b, 3b, 4b and 5b), the pattern is composed of two horizontal structures of opposite sign. In the third column (modes 4c, 5c and 6a), there are four structures located at the cavity corners. These patterns have already been observed by Koch (2005). Each column is related to different acoustic resonance modes: column 1 for the fundamental resonance mode $(0, 0)$, column 2 for the first longitudinal mode $(1, 0)$ and column 3 for the first longitudinal and depth mode $(1, 1)$. Figure 13 is analogous to figure 12, but this

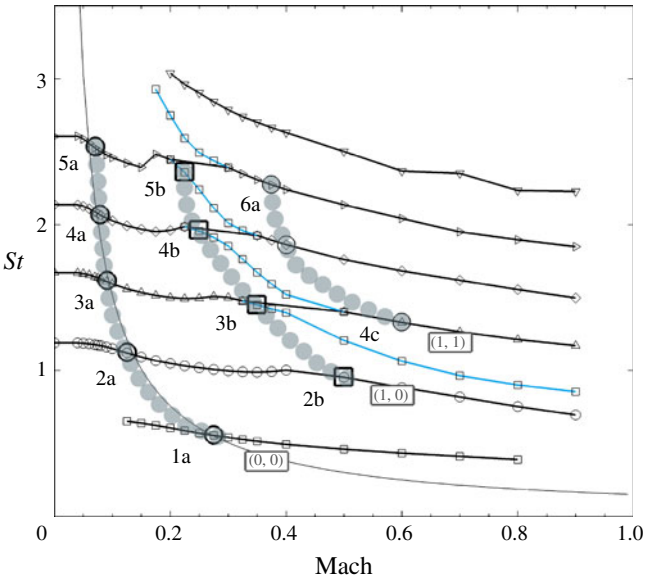

FIGURE 13. Unstable mode trajectories conserving the pressure pattern inside the cavity (see figure 11). The grey shaded circles represent the branches keeping the same pressure pattern inside the cavity, the lines with symbols are the branches with a constant number of structures (k) in the shear layer (see figure 12) and the blue branches, the transition branches. The black solid line refers to the East curve describing the fundamental acoustic resonance mode (equation (4.3)).

time, the grey shaded circles highlight the eigenmodes conserving the same pressure pattern inside the cavity. Note that each resonant curve (grey shaded circles) contains stable and unstable global modes, even though only the latter have been represented. We observe a good agreement between the East curve (equation (4.3)) (black solid line) and the branch related to the fundamental resonance mode $(0, 0)$ (grey shaded circles), retrieving the results obtained by Koch (2005). The black lines with symbols in figure 13 indicate the aeroacoustic feedback branches (k-branches) identified in figure 12. It is seen that the locations of the growth rate maxima (large open symbols along branch $(0, 0)$) match well with the intersections between the k branches and the East curve (equation (4.3)) describing the fundamental acoustic resonance mode (black solid line). As the Mach number is increased, the interchange of trajectories occurs just after having reached modes 2b, 3b, 4b and 5b of branch $(1, 0)$. It seems then that branch $(1, 0)$ triggers the branch switching phenomenon (see blue lines with symbols connecting different k branches).

4.3. *Link between incompressible and compressible regimes*

Figure 14 shows, for three different Mach numbers ($M = 0$ (a,d), $M = 0.4$ (b,e) and $M = 0.8$ (c,f)), two (x, t) diagrams of the pressure of the global modes lying on branch $k = 3$. In the first column (a–c), the pressure line is obtained on the cavity mouth at $y = 0$, between $x = -1$ and $x = 1.9$, while in the second column (d–f), the pressure line is extracted inside the cavity at $y = -0.25$.

There are three important regions in these diagrams, outlined by dashed vertical lines: the upstream region ($x \leqslant 0$), the cavity region ($0 \leqslant x \leqslant 1$) and the downstream region ($x \geqslant 1$). To understand these diagrams, we focus on the elongated blue line

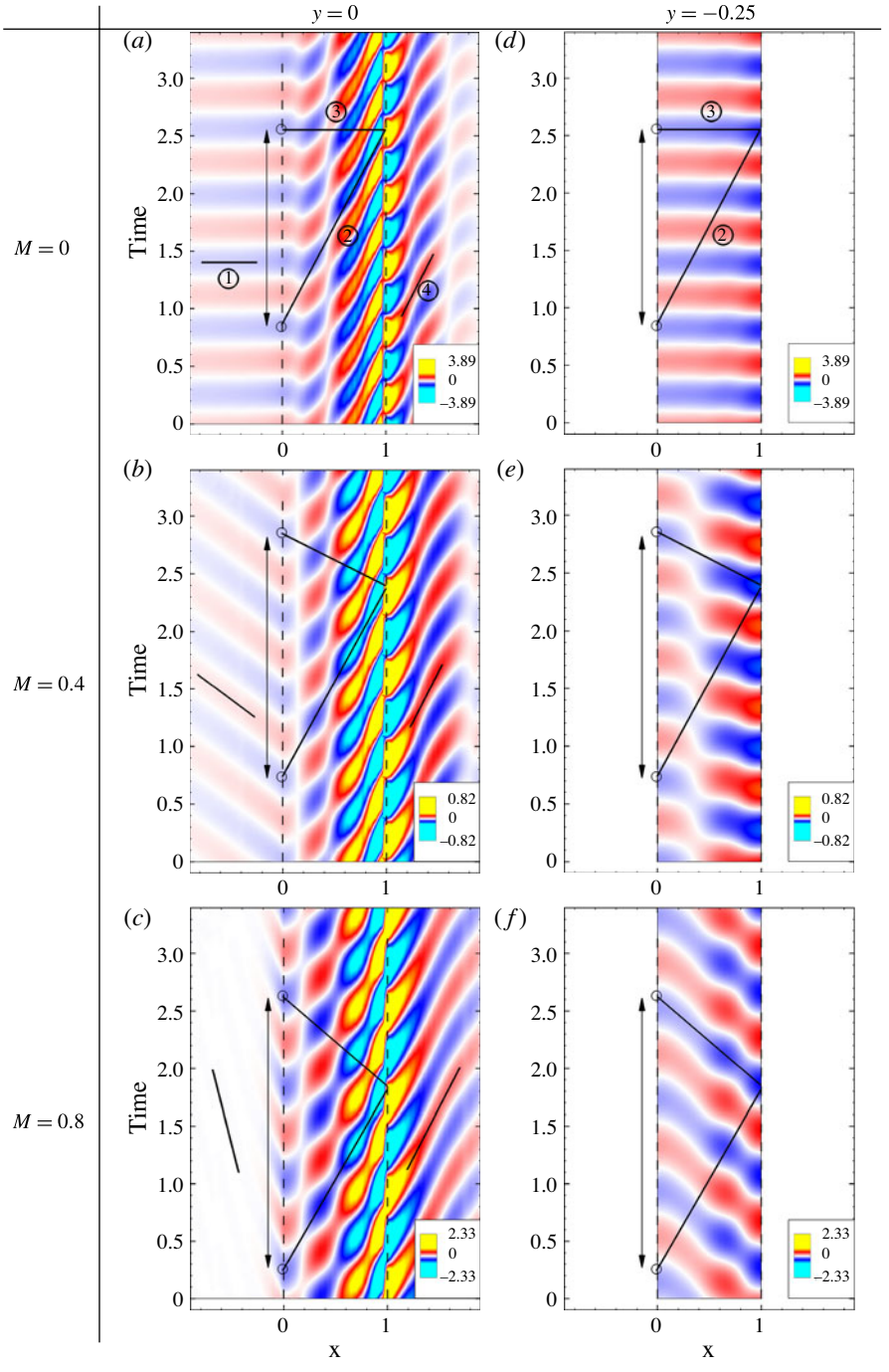

FIGURE 14. Spatiotemporal diagrams of the global modes belonging to branch $k = 3$, showing the pressure extracted on a segment at $y = 0$ between $x = -1$ and $x = 1.9$ (first column), and on a segment at $y = -0.25$ between $x = 0$ and $x = 1$ (second column). Three Mach numbers are presented: $M = 0$ (a,d), $M = 0.4$ (b,e) and $M = 0.8$ (c,f). The circled numbers refer to the slopes presented in table 2.

	①	②	③	④
$M = 0$	$-\infty$	0.57	$-\infty$	0.57
$M = 0.4$	-1.5	0.61	-2.37	0.57
$M = 0.8$	-0.25	0.64	-1.5	0.57

TABLE 2. Slopes of the different segment lines in figure 14. Negative (respectively, positive) values designate upstream (respectively, downstream) propagation of the pressure waves. The speed of the vortical structures is given in the third column: these values are seen to be close to the value $\kappa = 0.61$ that was used in figure 12 for the representation of mechanism I branches (black solid lines).

patterns, corresponding to the evolution over time of a pressure minimum. The slope of each of these line patterns corresponds to the velocity of the pressure waves, negative if they propagate upstream and positive in the other case. They can be of a hydrodynamic type, when describing a vortex centre, or acoustic. First, vortical structures are created at the cavity LE ($x = 0$). Looking at the diagrams at $y = 0$, we observe that these structures propagate downstream (positive slope) in the cavity and downstream regions. These propagation speeds (slopes of segments ② and ④) are only weakly influenced by the Mach number, the vortical structures being convected by the velocity field. At the cavity TE ($x = 1$), the vortices are distorted and hooked some time on the corner. Second, the vortices impinging on the cavity TE ($x = 1$) constitute an acoustic source emitting acoustic pressure waves in all directions (see § 4.4). Thus, upstream from the cavity TE ($x \leqslant 1$), the acoustic pressure waves propagate upstream and display negative speeds. In the upstream region, only acoustical structures are present and we retrieve the observations made in § 3.1 concerning the pressure wave speed in this region, $\mathrm{d}x/\mathrm{d}t = 1 - 1/M$, described by segment line ①. All slope values are given in table 2. In the cavity region, since the line $y = -0.25$ is below the shear layer, the pressure waves at this altitude no longer account for the downstream propagating vortices, but rather only for the upstream propagating acoustic pressure waves. This is why the slope of the elongated blue line patterns is negative inside the cavity. At $y = 0$, the acoustic pressure waves display weak amplitudes compared with the low-pressure regions associated with the vortices. They are therefore barely visible at the cavity mouth and they only modulate the amplitude of the downstream propagating low-pressure regions.

The type of representation in figure 14 allows us to describe an entire feedback loop physically. In each case, the circles on the vertical dashed line at $x = 0$ mark the beginning and the end of three periods, as the observed modes are lying on branch $k = 3$. At the lowest circle (earliest time), a vortex is generated at the cavity LE. It propagates along segment line ② up to the cavity TE. This travelling speed corresponds to the constant κ of (4.1) and is only weakly influenced by the Mach number. Once the cavity TE is reached, the vortical structure generates a pressure pulse after some delay. This time delay could correspond to the constant γ of (4.1), but is hardly visible here. Conversely, the feedback acoustic pressure wave (segment line ③) is really influenced by the Mach number: as the Mach number is increased, the travelling time of the feedback pressure wave increases also (see table 2). These feedback pressure waves may easily be observed at $y = -0.25$, an altitude at which they are not disturbed by the travelling vortices located just above in the shear layer. This illustrates why, following each k-branch of the aeroacoustic feedback mechanism (figure 12), the frequency is decreasing as a function of the Mach number.

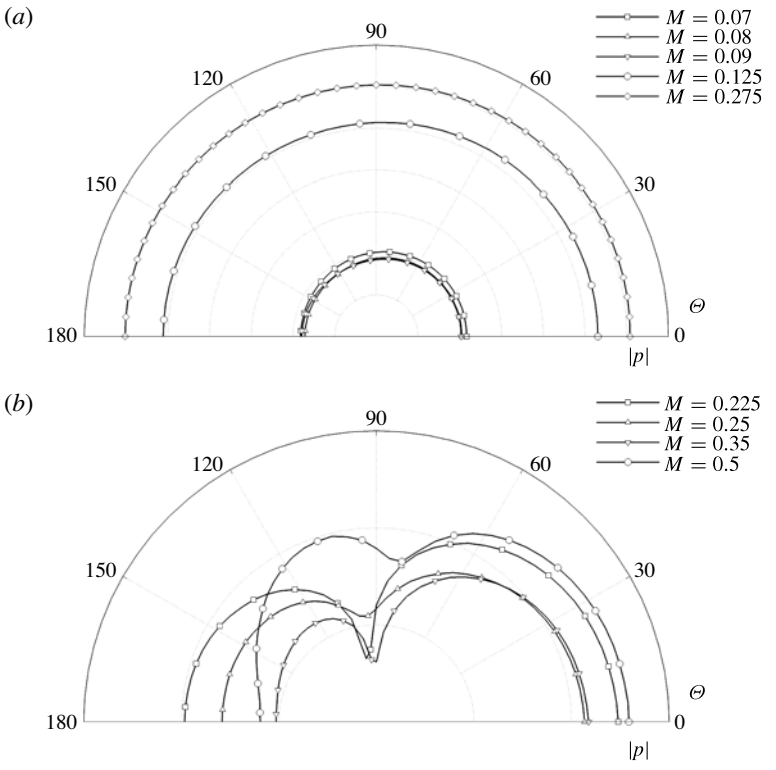

FIGURE 15. Acoustic polar directivity shapes of the global modes belonging to branches (0, 0) (*a*) and (1, 0) (*b*), calculated on a semicircle of radius $10L$ centred at the cavity TE.

Finally, this figure clearly shows that the same instability mechanism is at play for $M = 0$ and $M > 0$. Differences are only observed in the return speed of the feedback pressure wave (infinite for $M = 0$ and finite for $M > 0$), yet the overall picture is the same.

4.4. *Influence of the Mach number on the directivity*

In this part, we focus on the influence of the Mach and Strouhal numbers on the acoustic polar directivity of the unstable global modes. For this, we analyse the modulus of the pressure $|\hat{p}_1|$ along a circle of radius 10 centred at the cavity TE. A polar coordinate system is used and the polar angle $\Theta = 0°$ refers to the horizontal line oriented downstream (see figure 1). The radial coordinate corresponds to the pressure modulus represented in a logarithmic scale. It is important to note that the amplitude of the global modes being arbitrary, only the shape of the curve is of interest and not its overall amplitude.

In figure 15, we analyse the polar directivity along branches (0, 0) (figure 15*a*) and (1, 0) (figure 15*b*) (see figure 13). For each mode lying on curve (0, 0), a characteristic monopolar source is observed while on curve (1, 0), the directivity shapes are essentially dipolar. Referring back to figure 11, these polar directivities are in accordance with the acoustic resonance mode observed in the cavity: we observe a uniform pattern for branch (0, 0) yielding a monopolar directivity, and a pattern composed by two horizontal structures for branch (1, 0) yielding a dipolar directivity.

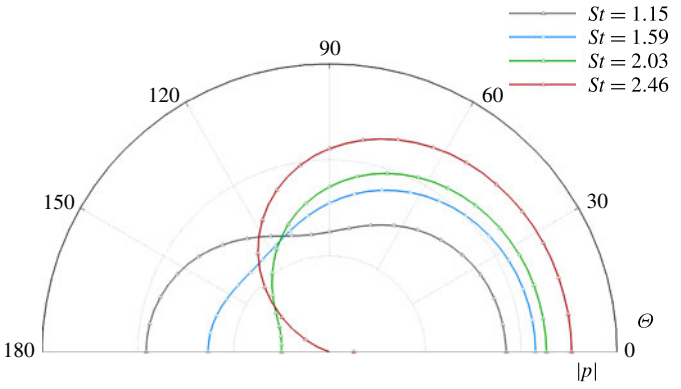

FIGURE 16. Acoustic polar directivity at $M = 0.1$, calculated on a semicircle of radius $10L$ centred at the cavity TE.

In figure 16, we analyse the directivity of the four unstable global modes obtained at $M = 0.1$ (see the diamonds in figure 7*a*). These global modes are identified by their frequency $St = 1.15, 1.59, 2.03$ and 2.46. It is observed that the directivity shape switches from a dipole at small Strouhal number ($St = 1.15$) to a monopole at higher Strouhal numbers ($St = 2.03$ and 2.46). These results are in accordance with the studies led by Howe (2004) at $M = 0.1$. The lowest mode characterized by $St = 1.15$ is clearly below the resonance frequency of branch $(0, 0)$. Therefore, the noise is only generated by the impinging shear layer (mechanism I) on the trailing edge and the directivity shape is dipolar (Curle 1955; Blake 1986). The second mode displays a frequency $St = 1.59$ closer to the resonant frequency $St_3(M = 0.1) = 1.52$ and is therefore closer to a monopole. For the two other modes ($St = 2.03$ and 2.46), the directivity pattern is oriented downstream.

Increasing the Mach number on branch $k = 2$ in figure 12, we obtain the directivity patterns sketched in figure 17(*a,b*). Figure 17(*a*) corresponds to low Mach numbers ($0.05 \leqslant M \leqslant 0.4$) while figure 17(*b*) relates to high Mach numbers ($0.4 \leqslant M \leqslant 0.9$). At very low Mach numbers ($M < 0.1$), the dipole source predominates. There is no acoustic resonance and the directivity shape is driven by the feedback aeroacoustic mechanism I. Around $M = 0.1$, it is seen in figure 13 that the frequency of the eigenmode on branch $k = 2$ crosses the acoustic resonance curve $(0, 0)$. Hence, the monopole source gains the upper hand peaking more in the downstream direction. For $M = 0.5$, a clear dipolar structure is observed again, as already shown in figure 15(*b*). Between $M = 0.1$ and $M = 0.5$, the directivity therefore moves progressively from a monopole to a dipole. Two acoustic sources therefore coexist: one at the cavity TE related to mechanism I and one inside the cavity linked to mechanism II. At even higher Mach numbers, the directivity pattern exhibits two main lobes, growing in the wall-normal and downstream directions, which flatten in the flow direction as the Mach number is increased.

Note that the shear layer itself is a quadrupole source, but its contribution to noise generation is negligible in comparison with the other acoustic sources mentioned above.

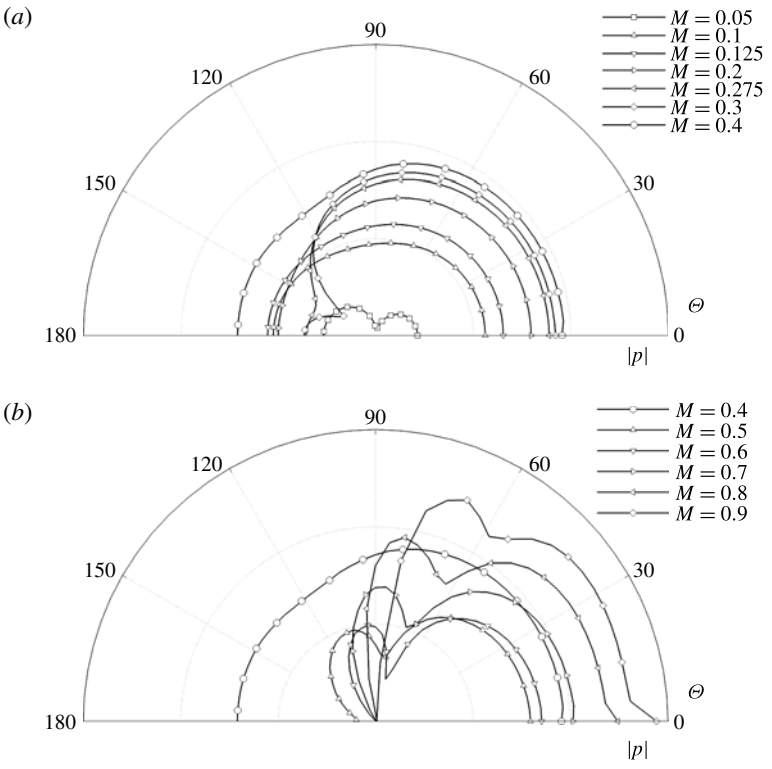

FIGURE 17. Acoustic polar directivity of the global modes belonging to trajectory $k = 2$ in figure 12, at low (*a*) and high Mach numbers (*b*), calculated on a semicircle of radius $10L$ centred at the cavity TE.

5. Discussion

The interaction phenomenon between the feedback aeroacoustic and acoustic resonance mechanisms highlighted in this paper has already been observed in experiments and simulations, by monitoring acoustic pressure levels. Block (1976) studied the case of a deep cavity of length-to-depth ratio equal to 0.66 at low Mach numbers, until $M = 0.5$. Block analyses a pressure spectrum and observes several peaks (characterized by a Strouhal number and an amplitude) evolving as a function of the Mach number. The amplitude of these peaks is the greatest when the aeroacoustic feedback curves ($k = 1, 2$) cross the first acoustic resonance curve of East (equation (4.3)). Koch (2005) has identified (in the experiments by Rossiter (1964)) the interaction involving the longitudinal acoustic mode $(1, 0)$. This has been also observed in large eddy simulations (LESs) by Larcheveque *et al.* (2003) and in experiments by Forestier, Jacquin & Geffroy (2003).

We will now give a simple argument explaining why a growth rate peak may also correspond to a peak of acoustic power when considering the full nonlinear dynamics. In the case of a super-critical Hopf bifurcation, it is known that the saturation amplitude $|A|$ of an unstable global mode is proportional to the square root of its amplification rate σ (see equation (2.31) in the work by Sipp & Lebedev (2007)). The pressure flow field, at a dominant order, is written as $p = p_0 + A\mathrm{e}^{\mathrm{i}\omega t}\hat{p}_1$ with $|A| \approx \sqrt{\sigma}$ and where ω is the frequency of the global mode. Therefore, the amplitude

of the pressure oscillations is proportional to the quantity $\sqrt{\sigma}$. Following this 'crude' argument, a peak of acoustic power should be associated with a growth rate peak. However, when multiple global modes are unstable, the nonlinear interactions may yield a more complex picture. Yet, it is still reasonable to claim that the global mode that exhibits (at a given Mach number) the strongest growth rate σ_{max} (among all unstable global modes) should be observed in a simulation or an experiment.

At very low Mach numbers, the growth rate of the unstable global modes converges toward its incompressible value, which quantifies the intrinsic strength of the feedback aeroacoustic mechanism. In the present case, from figure 10, it is seen that, for $M = 0$, modes $k = 3, 4, 2, 5$ are respectively characterized (from strongest to lowest amplification rates) by $\sigma = 1.19$, $\sigma = 1.03$, $\sigma = 0.76$ and $\sigma = 0.35$ while modes $k = 1, 6$ are stable. Following the results of Meliga *et al.* (2010), the increase of the Mach number should dampen Kelvin–Helmholtz instabilities and thus the unstable global modes. We see that this becomes invalid in the presence of acoustic resonance mechanisms. Here, it is seen that, when acoustic resonances occur, the growth rate may be locally increased by values of about $\Delta\sigma \approx 0.3$–0.5 for modes $k = 3, 4, 2$ and even more for modes $k = 5, 6$. Hence, for a given Mach number $M > 0$, the strongest growth rate σ_{max} results from a complex balance between the intrinsic strength of the feedback aeroacoustic mechanism (given roughly by the amplification rate in the incompressible regime) and the overshoot in amplification rate induced by the acoustic resonance mechanism. For example, at $M = 0.1$, the dominant mode is still mode $k = 3$: this is both due to the intrinsic strength of mode $k = 3$ and to a slight increase of the amplification rate due to the vicinity of the fundamental acoustic resonance mode. At higher Mach numbers, the dominant modes may not necessarily be those strengthened by the acoustic resonance mechanism. This phenomenon is observed at $M = 0.5$: even though mode $k = 2$ is located on the acoustic resonance branch $(1, 0)$, it displays a lower growth rate (see figure 10*b*,*e*) than mode $k = 4$.

Concerning the frequency, we saw in figure 4(*a*) that the Strouhal number of the unstable modes is slightly reduced when L/θ_0 is increased. These results pertaining to the incompressible regime, the travelling velocity of the feedback pressure wave is infinite (see § 4.3), so that only the convection speed of the vortices can account for this frequency decrease (segment ② in figure 14). In § 4.3, we also observe that the Mach number influences the speed of the feedback acoustic pressure wave (segment ③). Thus, it appears that parameter L/θ_0 and the Mach number M both influence the frequency of the phenomenon: yet they modify distinct parts of the feedback loop.

In the incompressible regime, the hydrodynamic pressure p_I of the global modes is governed by the incompressible Navier–Stokes equations. For very low Mach numbers, the pressure p involved in the compressible Navier–Stokes equations scales as $p = 1 + \gamma M^2 p_I$ (with p_I normalized so that $p_I \to 0$ in the free stream). This scaling is only valid for hydrodynamic-induced motions, such as the motion associated with the global modes belonging to the Kelvin–Helmholtz branch, which exist at $M = 0$, and shows how the hydrodynamic pressure p_I relates to the true pressure p at low Mach numbers, in the compressible equations. In the case of very low Mach numbers, the pressure fluctuations are therefore very weak and the modes driven by mechanism I are barely visible, except if the response of the mode is enhanced by the acoustic resonance mechanism. In experiments, the pressure peaks are therefore mostly seen near the acoustic resonance frequencies, which led to the idea that tones were generated by mechanism II at low Mach numbers (Tam & Block 1978). In this paper, we suggest that it is still mechanism I that produces the instability, even though it is enhanced by mechanism II. This idea is also supported

by the experimental observations of Sarohia (1975) and Basley *et al.* (2011) in the incompressible regime, who confirmed the existence of a shear-layer mode in the absence of acoustic resonances.

6. Conclusions

First, a global stability analysis has been performed on an unconfined incompressible cavity at a low Reynolds number of 7500. Two-dimensional computations were carried out to vary important parameters such as the boundary-layer thickness L/θ_0 and the length-to-depth ratio L/D. It has been shown that parameter L/θ_0 has a strong influence on the global modes: as L/θ_0 increases, the instability is strengthened. Meanwhile, parameter L/D has a weak influence. This led us to choose a high value of L/θ_0 for the study of the influence of compressibility effects. The spectra of the unstable global modes have been compared for Mach numbers ranging from $M = 0$ to $M = 0.9$. By analysing the evolution of their frequencies (as a function of the Mach number), we have identified branches that represent the feedback aeroacoustic mechanism (Rossiter 1964) (mechanism I) and the acoustic resonance mechanism (East 1966; Tam 1976; Koch 2005) (mechanism II). Looking at the mode shapes, the number of vortical structures in the shear layer is conserved along the curves of mechanism I, while the pressure pattern inside the cavity is conserved along each curve of mechanism II. Concerning mechanism I, good agreement was found with (4.2) especially at a low Strouhal number. We have shown that the unstable global modes in the incompressible regime are continuously linked with those in the compressible regime, looking at their characteristics (frequencies, growth rates, mode shapes). This establishes that the Rossiter mechanism also describes instabilities in incompressible open cavity flows. Second, the modes along mechanism II branches coincide with modes displaying a local maxima in growth rate. The positions of these maxima coincide with the locations where both mechanisms I and II are interacting. Therefore, a global stability analysis captures the feedback aeroacoustic mechanism, the resonance acoustic mechanism and their interactions. As a conclusion, the following picture emerges. The potential of the instability is given at $M = 0$, the Kelvin–Helmholtz instability on the shear layer being the engine of the instability with the hydrodynamic pressure feedback strengthening this mechanism. When increasing the Mach number, two antagonist mechanisms are at play for the amplification rate: (1) the Kelvin–Helmholtz instabilities should be slightly stabilized according to the physical mechanism described by Miles (1958), Pavithran & Redekopp (1989), Meliga (2008) and Meliga *et al.* (2010); (2) when acoustic resonance occurs, i.e. when the frequencies of the two mechanisms I and II match, an overshoot in the amplification rate curve is seen. Concerning the frequency, the Mach number determines the speed of the pressure feedback wave, which explains why the Strouhal number of the unstable global modes decreases with the Mach number. Let us make a final comment on the influence of the length-to-depth ratio L/D on the dynamics. The acoustic resonance modes being strongly dependent on the cavity geometry, the length-to-depth ratio L/D is therefore an important parameter when compressible governing equations are considered. On the other hand, as mentioned above, when the incompressible regime is considered, parameter L/D is less important.

Concerning the directivity analysis, we have retrieved the results from Howe (2004) at $M = 0.1$: the acoustic polar directivity evolves from that of a dipole at a low Strouhal number to a monopole at higher frequencies. By observing the evolution of the directivities along branch $k = 2$, we have observed that the directivity is monopolar

at the crossing of the first resonance curve $(0, 0)$ ($M \approx 0.1$), and clearly dipolar at the crossing of the resonance curve $(1, 1)$ ($M \approx 0.5$). In this study, the directivity shape seems to be linked to the pressure pattern inside the cavity when acoustic resonance occurs. If not, the directivity is dipolar in accordance with the dipolar shape induced by the impinging shear layer on the cavity TE.

Supplementary movies

Supplementary movies are available at http://dx.doi.org/10.1017/jfm.2012.563.

Appendix A. Three-dimensional linear dynamics in the incompressible regime

In this appendix, we study for $M = 0$ the three-dimensional perturbations, that were discovered by Brès & Colonius (2008) for $M > 0$. The disturbance is sought in the form

$$\boldsymbol{q}_1(x, y, z, t) = \hat{\boldsymbol{q}}_1(x, y)\mathrm{e}^{(\sigma+\mathrm{i}\omega)t+\mathrm{i}\beta z}, \tag{A 1}$$

where β designates the real transverse wavenumber; β is therefore a parameter of the present stability analysis.

Figure 18 shows the growth rate (a) and Strouhal number (b) of the most unstable three-dimensional mode as a function of the transverse wavelength $\lambda = 2\pi/\beta$ for different boundary-layer thicknesses L/θ_0. The symbols are the same as in figure 4 (filled symbols refer to case $L/D = 1$ while open symbols relate to case $L/D = 2$). All of the cases shown here are three-dimensionally unstable. Looking at the filled symbols, the influence of L/θ_0 is similar to that observed in § 2.2.2: the instability strengthens with L/θ_0 but less than with the two-dimensional mechanism. Increasing the length-to-depth ratio strengthens the three-dimensional instabilities, and renders high wavelength perturbations λ more unstable in the case $L/\theta_0 = 231$. Concerning figure 18(b), all of the unstable modes display very low frequencies compared with the two-dimensional instabilities, and increasing L/D causes a global decrease of the frequencies except for $\lambda \approx 1$, and for $\lambda \geqslant 3$ in the case $L/\theta_0 = 52.7$. For $L/\theta_0 = 231$ and $L/D = 2$, at low spanwise wavelengths λ, the unstable modes are even non-oscillating ($St = 0$).

The same conclusions were observed in the work by Brès & Colonius (2008): for two-dimensional and three-dimensional disturbances, parameter L/θ_0 has an important influence on the global mode stability, whereas varying the length-to-depth ratio (L/D) has little effect on the maximum growth rate level, but affects strongly the frequency of the modes. The authors have also observed that three-dimensional modes are essentially independent of the Mach number until $M = 0.6$.

Appendix B. Damping function determination

This appendix aims at explaining how the damping function is obtained. Considering the flow coming from the left of the domain and an acoustic source located at the cavity TE, the wave speed is not the same in all directions. For $x \leqslant x_{-\infty}$, the non-dimensional wave speed is $c = 1 - 1/M$, for $x \geqslant x_\infty$, $c = 1 + 1/M$ and for $y \geqslant y_\infty$, $c = 1/M$. To illustrate the method, let us choose the horizontal damping between $x = x_\infty$ and $x = x_\infty + l_s$ (see figure 2). As mentioned in § 3, we added the damping term β at the right-hand side of (2.1). It is zero at the beginning of the sponge zone so that $\beta(x, y) = \alpha'(x - x_\infty)$. We consider a characteristic $x(t)$ such that $\mathrm{d}x/\mathrm{d}t = c$.

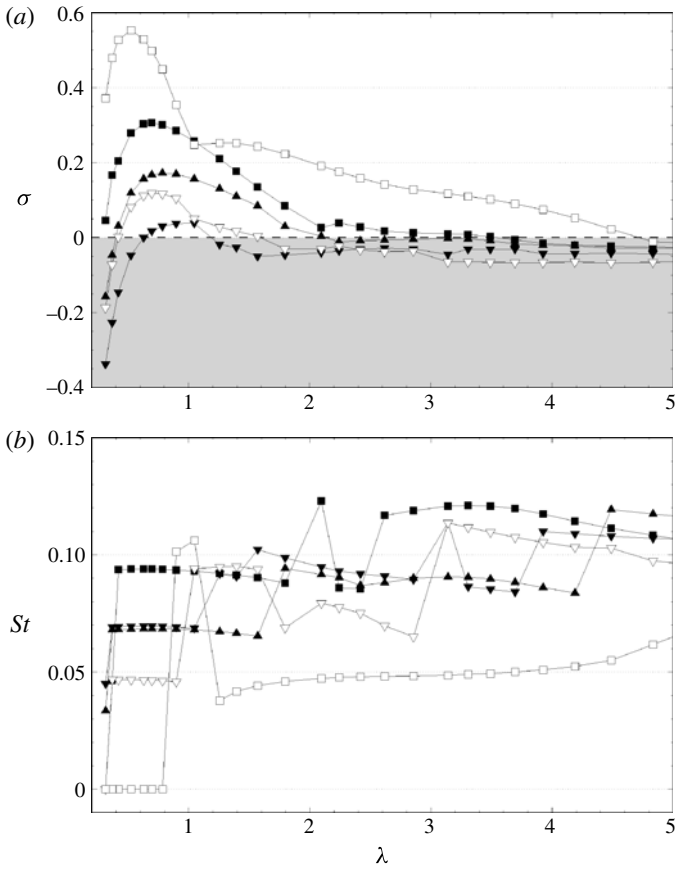

FIGURE 18. Eigenvalues of three-dimensional global modes in the incompressible regime as a function of the spanwise wavelength λ. (*a*) Plots of $L/D = 1$ and different values of L/θ_0, 231 (■), 110 (▲) and 52.7 (▼). (*b*) Plots of $L/D = 1$ and $L/\theta_0 = 231$ (■), $L/D = 2$ and $L/\theta_0 = 231$ (□), $L/D = 1$ and $L/\theta_0 = 52.7$ (▼), $L/D = 2$ and $L/\theta_0 = 52.7$ (▽).

Each component of $\boldsymbol{q}$ is damped as $\mathrm{d}q/\mathrm{d}t = -\beta q$. By substituting β and $\mathrm{d}t$, we obtain $\mathrm{d}q/q = -\alpha'(x - x_\infty)\mathrm{d}x/c$. Then, integrating this equation all over the sponge region of length l_s, yields $q/q_0 = \exp(-\alpha)$ with $\alpha = 0.5\alpha' l_s^2/c$. Finally, we have

$$\beta(x, y) = \frac{2c\alpha}{l_s^2}(x - x_\infty), \tag{B 1}$$

where α refers to the damping coefficient. In the present paper, α was set to four (a sensitivity test has been achieved in appendix C to show that the results do not depend on the precise value chosen for α).

Appendix C. Convergence studies

We used nine meshes to assess the convergence of the numerical simulations. Their characteristics are detailed in table 3. All of the meshes *M*2–*M*9 present variations of geometry or damping coefficient in comparison with mesh *M*1 used as the reference mesh. Here $x_{-\infty}$, x_∞, y_∞ correspond to the location of the inlet, outlet and upper

	$x_{-\infty}$	x_{∞}	y_{∞}	l_s	α'	n_t
M1	−50	100	33	150	4	1 119 022
M2	−50	100	30	150	4	1 159 906
M3	−60	100	30	150	4	1 133 627
M4	−50	80	30	150	4	1 088 996
M5	−50	100	30	160	4	1 135 948
M6	−50	100	20	150	4	1 045 152
M7	−50	100	25	150	4	1 069 192
M8	−50	100	25	150	4	1 156 416
M9	−50	100	30	150	3	1 119 022

TABLE 3. Different meshes used to validate the stability calculations. The grey cells highlight the parameters modified with respect to the reference mesh $M1$.

	σ	Strouhal
M1	1.4381	1.7609
M2	1.4377	1.7607
M3	1.4383	1.7609
M4	1.4386	1.7610
M5	1.4377	1.7607
M6	1.4381	1.7607
M7	1.4376	1.7607
M8	1.4384	1.7609
M9	1.4382	1.7610

TABLE 4. Comparison of the eigenvalue calculations for the different meshes. We consider the most unstable mode at $M = 0.5$.

boundaries, respectively, and l_s to the sponge zone size. The damping coefficient α is defined in appendix D and n_t is the number of triangles. In table 4, we compare for all meshes the most unstable eigenvalue obtained at $M = 0.5$. Results obtained in terms of growth rate and frequency show a good convergence for all cases. Yet, this convergence test only concerns variations of geometric parameters, the order of the spatial discretization being still the same.

A second convergence test is offered in figure 19, where the unstable global modes at $M = 0.7$ are presented using the same mesh $M1$ but for different discretization strategies. We compare results obtained with (P1, P1b, P1b, P1) elements (square symbols), (P2, P2, P2, P2) elements (circle symbols) and with the reference (P1, P2, P2, P1) elements (delta symbols). The finite elements P1 and P2 refer respectively to first- and second-degree polynomials: in a triangle, there are three degrees of freedom with P1 elements and six degrees of freedom for P2 elements. Element P1b has an additional degree of freedom with respect to the P1 element and displays four degrees of freedom in a triangle. Hence, we obtain 4 486 112 degrees of freedom for a (ρ, u, v, T) unknown with (P1, P1b, P1b, P1) elements, 5 610 144 degrees of freedom with (P1, P2, P2, P1) elements and 8 972 220 degrees of freedom for (P2, P2, P2, P2) elements. Overall speaking, the (P1, P1b, P1b, P1) elements yield first-order discretizations while the (P2, P2, P2, P2) strategy is second order. The (P1, P2, P2, P1) strategy is second order for the velocity fields and only first order for ρ and T. The inversion of the matrices involved in the computation of the base flows and of

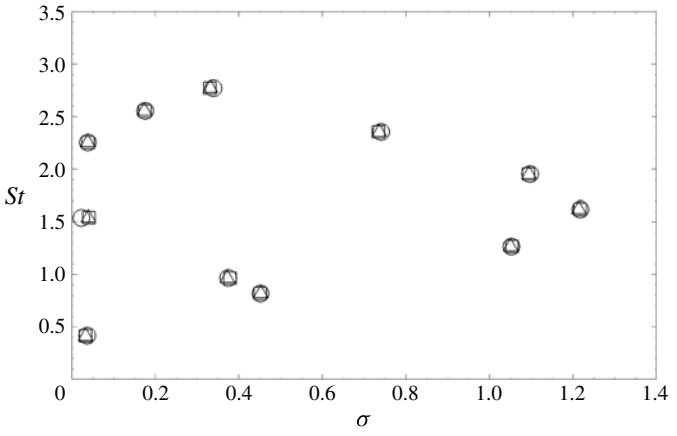

FIGURE 19. Global spectrum at $M = 0.7$ for mesh $M1$, but for different discretization strategies: (□), (P1, P1b, P1b, P1); (△), (P1, P2, P2, P1); and (○), (P2, P2, P2, P2).

Mach number	δ_0	Re_{δ_0}
0	0.01203	90.2
0.2	0.01224	91.8
0.4	0.01233	92.5
0.6	0.01248	93.6
0.8	0.01264	94.8

TABLE 5. Displacement thickness at $x = 0$ and Reynolds numbers based on it for different Mach numbers.

the spectra becomes prohibitively expensive for the (P2, P2, P2, P2) strategy: therefore, only a convergence test has been achieved here to show that all elements yield the same results. It is seen in figure 19 that even the high-frequency modes are well captured by the (P1, P1b, P1b, P1) elements and the (P1, P2, P2, P1) reference elements.

Appendix D. Influence of the Mach number on the displacement thickness

This appendix gives the evolution of the displacement thickness (δ_0) and the associated Reynolds number (Re_{δ_0}) at the cavity LE ($x = 0$) as a function of the Mach number (table 5). We observe that both values are only very weakly affected by the Mach number.

REFERENCES

AHUJA, K. K. & MENDOZA, J. 1995 Effects of cavity dimensions, boundary layer, and temperature on cavity noise with emphasis on benchmark data to validate computational aeroacoustic codes. *NASA Contractor Report* 4653.

ALVAREZ, J. O., KERSCHEN, E. J. & TUMIN, A. 2004 A theoretical model for cavity acoustic resonances in subsonic flow. *AIAA Paper* 2845.

AMESTOY, P. R., DUFF, I. S., KOSTER, J. & L'EXCELLENT, J.-Y 2001 A fully asynchronous multifrontal solver using distributed dynamic scheduling. *SIAM J. Matrix Anal. Applics* **23** (1), 15–41.

BARBAGALLO, A., SIPP, D. & SCHMID, P. 2009 Closed-loop control of an open cavity flow using reduced order models. *J. Fluid Mech.* **641**, 1–50.

BARKLEY, D. 2006 Linear analysis of the cylinder wake mean flow. *Europhys. Lett.* **75** (5), 750.

BASLEY, J., PASTUR, L. R., LUSSEYRAN, F., FAURE, T. M. & DELPRAT, N. 2011 Experimental investigation of global structures in an incompressible cavity flow using time-resolved piv. *Exp. Fluids* **50** (4), 905–918.

BILANIN, A. J. & COVERT, E. E. 1973 Estimation of possible excitation frequencies for shallow rectangular cavities. *AIAA J.* **11** (3), 347–351.

BLAKE, W. K. 1986 *Mechanics of Flow-induced Sound and Vibration*. Academic.

BLOCK, P. J. W. 1976 Noise response of cavities of varying dimensions at subsonic speeds. *Tech. Rep.* D-8351. NASA Tech. Note.

BRÈS, G. A. & COLONIUS, T. 2008 Three-dimensional instabilities in compressible flow over open cavities. *J. Fluid Mech.* **599**, 309–339.

CANDEL, S. M. 1992 Combustion instabilities coupled by pressure waves and their active control. In *Symposium (International) on Combustion*, vol. 24. pp. 1277–1296. Elsevier.

CHEDEVERGNE, F., CASALIS, G. & FÉRAILLE, T. 2006 Biglobal linear stability analysis of the flow induced by wall injection. *Phys. Fluids* **18**, 014103.

COLONIUS, T. 2004 Modelling artificial boundary conditions for compressible flow. *Annu. Rev. Fluid Mech.* **36**, 315–345.

CRAIK, A. D. D. 1988 *Wave Interactions and Fluid Flows*. Cambridge University Press.

CROUCH, J. D., GARBARUK, A. & MAGIDOV, D. 2007 Predicting the onset of flow unsteadiness based on global instability. *J. Comput. Phys.* **224** (2), 924–940.

CROUCH, J. D., GARBARUK, A., MAGIDOV, D. & TRAVIN, A. 2009 Origin of transonic buffet on aerofoils. *J. Fluid Mech.* **628**, 357.

CURLE, N. 1955 The influence of solid boundaries upon aerodynamic sound. *Proc. R. Soc. Lond. Ser.* A. *Mathematical and Physical Sciences* **231** (1187), 505–514.

EAST, L. F. 1966 Aerodynamically induced resonance in rectangular cavities. *J. Sound Vib.* **3**, 277–287.

FORESTIER, N., JACQUIN, L. & GEFFROY, P. 2003 The mixing layer over a deep cavity at high-subsonic speed. *J. Fluid Mech.* **475**, 101–145.

GHARIB, M. & ROSHKO, A. 1987 The effect of flow oscillations on cavity drag. *J. Fluid Mech.* **177**, 501–530.

HOWE, M. S. 2004 Mechanism of sound generation by low Mach number flow over a wall cavity. *J. Sound Vib.* **273** (1–2), 103–123.

JACKSON, C. P. 1987 A finite-element study of the onset of vortex shedding in flow past variously shaped bodies. *J. Fluid Mech.* **182** (1), 23–45.

KOCH, W. 2005 Acoustic resonances in rectangular open cavities. *AIAA J.* **43** (11), 2342–2349.

KRISHNAMURTY, K. 1956 Sound radiation from surface cutouts in high speed flow. PhD thesis, California Institute of Technology.

LARCHEVEQUE, L., SAGAUT, P., MARY, I., LABBÉ, O. & COMTE, P. 2003 Large-eddy simulation of a compressible flow past a deep cavity. *Phys. Fluids* **15**, 193.

LEHOUCQ, R. B. 1995 Deflation techniques for an implicitly re-started arnoldi iteration. *Tech. Rep*. DTIC document.

MACK, C. J., SCHMID, P. J. & SESTERHENN, J. L. 2008 Global stability of swept flow around a parabolic body: connecting attachment-line and crossflow modes. *J. Fluid Mech.* **611** (1), 205–214.

MELIGA, P. 2008 A theoretical approach for the onset and control of unsteadiness in compressible afterbody flows. PhD thesis, Ecole Polytechnique.

MELIGA, P., SIPP, D. & CHOMAZ, J. M. 2010 Effect of compressibility on the global stability of axisymmetric wake flows. *J. Fluid Mech.* **660**, 499–526.

MERY, F. & CASALIS, G. 2011 Innovative tool for realistic cavity flow analysis: global stability. In *Proceedings of the Sixth International Conference on Computational Fluid Dynamics, ICCFD6, St Petersburg, Russia, on July 12–16 2010*, p. 449 Springer.

MILES, J. W. 1958 On the disturbed motion of a plane vortex sheet. *J. Fluid Mech.* **4** (Pt 5), 538–552.

MONKEWITZ, P. A., HUERRE, P. & CHOMAZ, J. M. 1993 Global linear stability analysis of weakly non-parallel shear flows. *J. Fluid Mech.* **251**, 1–20.

PAVITHRAN, S. & REDEKOPP, L. G. 1989 The absolute-convective transition in subsonic mixing layers. *Phys. Fluids* A: *Fluid Dynamics* **1**, 1736.

PLUMBLEE, H. E., GIBSON, J. S. & LASSITER, L. W. 1962 A theoretical and experimental investigation of the acoustic response of cavities in aerodynamic flow. *Tech. Rep.* WADD-TR-62-75. U.S. Air Force Rep.

ROBINET, J. C. 2007 Bifurcations in shock-wave/laminar-boundary-layer interaction: global instability approach. *J. Fluid Mech.* **579** (1), 85–112.

ROCKWELL, D. & KNISELY, C. 1979 The organized nature of flow impingement upon a corner. *J. Fluid Mech.* **93** (03), 413–432.

ROCKWELL, D. & NAUDASCHER, E. 1978 Review self-sustaining oscillations of flow past cavities. *J. Fluids Engng* **100**, 152.

ROCKWELL, D. & SCHACHENMANN, A. 1982 Self-generation of organized waves in an impinging turbulent jet at low Mach number. *J. Fluid Mech.* **117** (1), 425–441.

ROSSITER, J. E. 1964 Wind-tunnel experiments on the flow over rectangular cavities at subsonic and transonic speeds. *Tech. Rep.* Aero. Res. Counc. R. & M.

ROWLEY, C. W., COLONIUS, T. & BASU, A. J. 2002 On self-sustained oscillations in two-dimensional compressible flow over rectangular cavities. *J. Fluid Mech.* **455**, 315–346.

SAROHIA, V. 1975 Experimental and analytical investigation of oscillations in flows over cavities. PhD thesis, California Institute of Technology.

SAROHIA, V. 1977 Experimental investigation of oscillations in flows over shallow cavities. *AIAA J.* **15** (7), 984–991.

SCHMID, P. J. & HENNINGSON, D. S. 2001 *Stability and Transition in Shear Flows. Applied Mathematical Sciences, vol. 142*, Springer.

SIPP, D. & LEBEDEV, A. 2007 Global stability of base and mean flows: a general approach and its applications to cylinder and open cavity flows. *J. Fluid Mech.* **593**, 333–358.

SIPP, D., MARQUET, O., MELIGA, P. & BARBAGALLO, A. 2010 Dynamics and control of global instabilities in open-flows: a linearized approach. *Appl. Mech. Rev.* **63**, 030801.

TAM, C. K. W. 1976 The acoustic modes of a two-dimensional rectangular cavity. *J. Sound Vib.* **49**, 353–364.

TAM, C. K. W. & BLOCK, P. J. W. 1978 Tones induced by flow over cavities. *J. Fluid Mech.* **89**, 373–399.

THEOFILIS, V. 2003 Advances in global linear instability analysis of nonparallel and three-dimensional flows. *Prog. Aerosp. Sci.* **39** (4), 249–316.

YANG, Y., ROCKWELL, D., LAI-FOOK CODY, K. & POLLACK, M. 2009 Generation of tones due to flow past a deep cavity: effect of streamwise length. *J. Fluids Struct.* **25** (2), 364–388.